
FACTORS: FACTORIAL APPROXIMATION FOR COMPLEMENTARY TWO-FACTOR OPTIMIZATION WITH RISK-AWARE SCORING

Dongseok Kim, Wonjun Jeong, Gisung Oh
Department of Computer Engineering
Gachon University
Seongnam-si, Gyeonggi-do, South Korea
{jkds5920, tp04045, eustia}@gachon.ac.kr

ABSTRACT

We propose FACTORS, a framework that combines design of experiments with Shapley decomposition to address performance and stability issues that are sensitive to combinations of training factors. Our approach consistently estimates main effects and two-factor interactions, then integrates them into a risk-adjusted objective function that jointly accounts for uncertainty and cost, enabling reliable selection of configurations under a fixed budget. Effect estimation is implemented through two complementary paths: a plug-in path based on conditional means, and a least-squares path that reconstructs Shapley contributions from samples. These paths are designed to work complementarily even when design density and bias levels differ. By incorporating standardization of estimates, bias correction, and uncertainty quantification, our procedure ensures comparability across heterogeneous factor spaces and designs, while a lightweight search routine yields configurations within practical time even for large factor spaces. On the theoretical side, we provide error decompositions, sample complexity analysis, and upper bounds on optimality gaps. On the interpretive side, we summarize main effects and interactions in map form, highlighting adjustment priorities and safe improvement pathways. Across diverse datasets and design conditions, our approach improves rank preservation and optimal configuration identification, reduces decision-making risks, and offers a tuning foundation that delivers interpretable justification alongside stable performance gains even under budget constraints.

Keywords Design of Experiments · Explainable AI · Factorial Design · Shapley Values · Uncertainty Quantification

1 Introduction

1.1 Motivation

In practical machine learning operations, the most frequently repeated activity is not changing the data itself but adjusting training factors such as learning rate, batch size, optimizer, regularization strength, and schedules. Performance, stability, and reproducibility are highly sensitive to combinations of these factors, yet current tuning is largely trial-and-error based, incurring substantial costs in time and resources. At the same time, organizations must operate models within frameworks of standards and regulations that demand reliability and accountability. The NIST AI Risk Management Framework [1] outlines risk management and trustworthiness characteristics across the entire lifecycle of design, development, and deployment. The OECD AI Principles [2] and the EU AI Act [3] require accountability, transparency, documentation, and control in the language of policy and law. ISO/IEC 23894 [4] and ISO/IEC 25059 [5] bind risk management and quality characteristics into common terminology and procedures that translate into operational rules for organizations. Our motivation begins here: explanation should not end with reports but must lead to concrete prescriptions for tunable design variables.

In production pipelines, data dependencies, configuration settings, and feedback loops are entangled, and small decisions often amplify long-term maintenance costs and variability. Several studies propose checklists, pipeline standardization,

and operational metrics to mitigate these risks [6, 7, 8, 9]. The implication is clear: signals at the factor level need to be systematically collected and linked to operational decision-making procedures.

From the perspective of reproducibility, it has been repeatedly observed that even for the same model, performance can vary substantially depending on seed choice, data difficulty, and evaluation protocol. Multiple studies point to systematic drops in performance on new test sets, nondeterminism in reinforcement learning, reporting practice issues, and reproducibility gaps in large-scale architecture searches [10, 11, 12]. A single objective function alone leads to unstable conclusions, underscoring the need for frameworks that decompose sources of variability and report them with confidence intervals and sample complexity. Only then can subsequent adjustments consistently yield improvements.

From a scaling perspective, quantitative relationships have been established showing that the balance among compute budget, number of data tokens, and model size governs performance. Several studies present such scaling laws, emphasizing that system and training factors are first-class design variables [13, 14]. Meanwhile, industry reports highlight that although adoption is spreading rapidly, a persistent gap remains between value realization and trust building. McKinsey & Company [15], PwC [16], and BCG [17] emphasize that operational maturity and trust frameworks are critical for translating investments into impact. Ultimately, effective explanations must go beyond showing internal model evidence; they must present actionable directions and priorities for adjusting design variables.

We therefore propose a procedure that combines design theory with Shapley-based decomposition to estimate the main effects and two-factor interactions of training factors, integrating them into an objective function that accounts for both risk and cost to identify optimal configurations. By reconstructing explanation as actionable signals rather than static reports, our approach provides a path to reproducible performance gains even under limited budgets.

1.2 Contributions

This paper proposes a framework that does not stop at explanatory reports but directly connects quantitative signals on training factors to the objective function and search procedure, leading to actionable improvements. The core idea is to combine design theory with Shapley-based decomposition to reliably estimate main and interaction effects of hyperparameters, and to derive optimal configurations that satisfy operational constraints. The specific contributions of this paper are as follows:

- **Formulation of the FACTORS framework** We introduce an integrated framework that combines factorial decomposition with Shapley-based attribution to define and estimate main-effect and interaction plots for hyperparameters and system factors. The formulation includes sample weighting and reference decompositions to ensure functionality under unbalanced logs and fractional designs.
- **Two-factor approximation and objective function** We approximate the performance function using main effects and two-factor interactions, and formalize an objective function that incorporates expected performance gains, uncertainty penalties, execution costs, and operational constraints. Standardization of effect estimates ensures comparability across different factor spaces and experimental designs.
- **Estimation procedure and uncertainty quantification** We present an estimation pipeline that includes bias correction, variance estimation, and confidence interval computation. We also provide sample complexity bounds to guide the experimental budget required for achieving a desired estimation error.
- **Optimal configuration solver** We design a search procedure that spans both discrete levels and discretized continuous levels, producing configurations that satisfy constraints under the proposed objective function. By combining lightweight heuristics such as graph-based dynamic programming and integer linear approximations, our solver delivers practical solutions even in large factor spaces.
- **Theoretical guarantees** We provide consistency results and error decompositions for the Shapley-based approximation, derive upper bounds on optimality gaps under the two-factor approximation, and summarize monotonicity and interpretability conditions for decision metrics.
- **Empirical validation** We systematically evaluate recovery accuracy of main and interaction effects, performance improvements from objective-based search, conservativeness of uncertainty measures, and robustness to design imbalance using synthetic datasets and public benchmarks.
- **Reproducibility** We release code, configuration files, execution scripts, and log summarization tools to ensure that all results in the paper can be reproduced with a single click.

2 Related Work

2.1 Design of Experiments and Machine Learning

Design of experiments has developed into a foundation for systematic, low-cost exploration and reliable estimation in computer experiments and machine learning. Sacks et al. [18] combined Gaussian process surrogates with experimental designs to efficiently predict computer code responses. McKay et al. [19] introduced Latin hypercube sampling to achieve uniform stratification in high-dimensional input spaces. Stein [20] analyzed the large-sample properties of such sampling methods, providing stronger theoretical justification. Plackett and Burman [21] established classical factorial designs that enable rapid screening of main effects among many factors. Morris [22] proposed the use of elementary effects to perform practical factor screening even for computationally expensive models.

Improvements in space-filling properties and orthogonality have also been steadily accumulated. Tang [23] proposed designs incorporating orthogonal arrays to control correlations across dimensions. Morris and Mitchell [24] quantified the space-filling quality of designs using the maximin distance criterion. Joseph et al. [25] introduced maximum projection designs that maintain uniform distributions across all low-dimensional projections, advancing modern quality standards for computer experiment designs.

These design strategies have been extended to surrogate-assisted search and expensive function optimization. Jones et al. [26] established the expected improvement criterion, showing that global improvements can be achieved with few evaluations. Shahriari et al. [27] provided a comprehensive review of Bayesian optimization, highlighting how various acquisition functions and uncertainty quantification complement experimental design. Snoek et al. [28] demonstrated that Gaussian process–based optimization delivers practical performance gains across diverse models and datasets.

When focusing on hyperparameter search in machine learning, the integration of design and search becomes more explicit. Bergstra and Bengio [29] showed theoretically and empirically that random search can be more efficient than grid search. Bergstra et al. [30] introduced procedures based on sequential density estimation to improve search adaptivity. Li et al. [31] proposed resource allocation strategies that enable fast and robust exploration. Falkner et al. [32] combined Hyperband with Bayesian optimization to ensure consistent performance in large-scale environments. Klein et al. [33] introduced a learning-based approach that balances cost and information by treating dataset size as a control variable. Kandasamy et al. [34] formalized trade-offs between low-cost approximations and high-fidelity evaluations through multi-fidelity optimization. Golovin et al. [35] released large-scale, platform-based optimization services, demonstrating automation in design execution and analysis.

2.2 Feature Attribution and the SHAP Family

Feature attribution has developed as an attempt to decompose black-box predictions into input dimensions to identify decision-making rationales. Ribeiro et al. [36] introduced LIME, a model-agnostic explanation method based on local linear approximations applicable to arbitrary classifiers. Lundberg and Lee [37] proposed SHAP, which reinterprets Shapley values axiomatically, unifying prior methods into a single framework with guarantees of consistency and local accuracy. Sundararajan et al. [38] introduced the axioms of sensitivity and implementation invariance, and proposed Integrated Gradients based on path integrals, providing stable attributions applicable to deep networks. Shrikumar et al. [39] presented DeepLIFT, which propagates differences from reference activations to enable efficient attribution in a single backward pass.

In the context of visual models, Bach et al. [40] formalized pixel-level relevance decomposition through LRP, while Selvaraju et al. [41] proposed gradient-weighted activation maps that offer localization explanations broadly applicable to CNN families. Smilkov et al. [42] reported SmoothGrad, a simple procedure that improves the visual sharpness of gradient-based saliency maps by adding noise to inputs and averaging. Fong and Vedaldi [43] treated input region removal as an optimization problem, establishing model-agnostic deletion-based explanations that identify meaningful regions. Zeiler and Fergus [44] proposed a classical approach to feature visualization using deconvolutional networks to analyze intermediate representations and failure modes.

Within the SHAP family, specialized algorithms for tree models and global interpretation tools have advanced rapidly. Lundberg et al. [45] introduced TreeSHAP, which computes Shapley values in polynomial time for trees, and developed interaction values and global combinations of local explanations, providing structured insights in clinical examples. Sundararajan and Najmi [46] showed that multiple Shapley-style attributions exist depending on path choices and background distributions, organizing principles for method selection. Sundararajan et al. [47] formalized the Shapley–Taylor index, which decomposes contributions up to interaction order k , extending interaction interpretability theoretically. Ribeiro et al. [48] proposed Anchors, a rule-based local explanation method that summarizes decision boundaries with high precision and stability.

Issues of feature dependence and global importance have also been addressed. Breiman [49] established permutation importance using out-of-bag errors, providing a practical standard for global variable importance. Altmann et al. [50] proposed a bias-corrected permutation importance estimator. Aas et al. [51] extended kernel SHAP by incorporating conditional distributions under correlated features, reducing distortions in explanations. Covert et al. [52] presented a unified framework for deletion-based explanations, deriving information-theoretic interpretability conditions to refine the connection between attribution and removal.

Research has also actively examined the fidelity and validity of explanation methods. Adebayo et al. [53] used tests such as weight randomization to show that some saliency methods may be insensitive to model and data, highlighting the need for rigorous benchmarks. Hooker et al. [54] introduced the Remove And Retrain metric to quantitatively assess how attribution estimates affect predictive performance.

2.3 Limits of Post-hoc XAI and the Gap to Actionability

Post-hoc explanations aim to show model decisions to humans, but whether these explanations faithfully reflect the model’s internal mechanisms and whether they lead to practical improvements are separate issues that have been repeatedly raised. Rudin [55] criticizes the practice of attaching post-hoc explanations to black-box models in high-stakes domains, arguing that such approaches fail to ensure accountability or improvements, and that interpretable models by design are a safer alternative.

Studies evaluating explanation quality consistently report gaps between visual plausibility and methodological faithfulness. Adebayo et al. [53] demonstrated through tests such as weight randomization that many saliency methods are insensitive to the underlying model and data. Hooker et al. [54] showed with the Remove And Retrain procedure that importance estimates from various methods may not differ significantly from random baselines.

Explanation fragility and manipulability have also emerged as critical limitations. Ghorbani et al. [56] showed cases where minor input perturbations drastically altered interpretation results. Dombrowski et al. [57] provided theoretical and empirical evidence that almost imperceptible perturbations can arbitrarily distort explanations. Slack et al. [58] demonstrated that LIME and SHAP can be fooled into concealing structural biases, highlighting vulnerabilities in explanation-driven debugging.

The distinction between plausibility and faithfulness is also conceptual. Jacovi and Goldberg [59] formally distinguished the two, noting that high plausibility does not imply faithfulness. Hase and Bansal [60] evaluated explanation validity through human prediction of model outputs, providing quantitative evidence that explanations often fail to aid as much as expected. Jain and Wallace [61] and Wiegrefe and Pinter [62] reached conflicting conclusions about whether attention mechanisms can serve as explanations, underscoring that definition and evaluation of explanations are context-dependent.

In human–AI collaboration, explanations have repeatedly failed to directly translate into improved behavior. Poursabzi-Sangdeh et al. [63] showed in a large preregistered study that increased model transparency does not necessarily improve the quality of human decisions. Bansal et al. [64] reported that providing explanations does not systematically enhance complementary performance between humans and AI. Wang et al. [65] concluded that explanation effects vary substantially depending on task and expertise, and often fail to meet desirable decision-making criteria. Recent surveys further argue that structural reasons prevent explanations from reliably inducing appropriate reliance and complementary performance.

Field studies of practitioners also highlight overreliance and misuse of interpretability tools. Kaur et al. [66] reported that data scientists often overtrust or misinterpret outputs from tools such as SHAP, concluding that explanations rarely translate into systematic procedures for model improvement.

2.4 Hyperparameter- and System-level SHAP

Attempts to quantify the contributions of hyperparameters and system-level factors have evolved along two main directions. The first is an approach that leverages design theory and hyperparameter search logs to decompose performance variance into main effects and low-order interactions. Hutter et al. [67] proposed functional ANOVA as a method to efficiently estimate hyperparameter importance. Extending this line into the Shapley framework, Wever et al. [68] formulated performance as a value function and derived both local and global importance using Shapley values and interaction indices.

The second direction combines sensitivity analysis with game theory to fairly allocate dependencies and interactions among inputs. Song et al. [69] formalized Shapley effects to address variance allocation problems under dependent inputs, and Aas et al. [51] extended kernel SHAP to dependent features to reduce distortions in explanations. Sundararajan et

al. [47] introduced indices that explicitly decompose contributions by interaction order, while Sundararajan and Najmi [46] summarized how different Shapley-style attributions arise depending on the choice of value function.

Another line of system-level attribution focuses on quantifying the contributions of data and internal components. Ghorbani and Zou [70] measured the contribution of each training data point to predictive performance using Shapley values. Kwon and Zou [71] relaxed the efficiency axiom by introducing Beta Shapley, reducing noise in data value estimation. Pruthi et al. [72] proposed TracIn, which approximates data influence at scale by tracing training trajectories, while Koh and Liang [73] extended influence functions to modern settings to track data item contributions to predictions. At the model-internal level, Ghorbani and Zou [74] defined neuron-level contributions via Shapley values.

Systematic effects of training recipes and resource configurations on performance have also been documented in large-scale experiments. Goyal et al. [75] demonstrated that scaling rules for batch size and learning rate can reduce training time in large-scale distributed learning without loss of accuracy. Smith et al. [76] proposed increasing batch size in place of learning-rate decay to achieve equivalent generalization curves. Keskar et al. [77] analyzed how large batches converge to sharp minima, potentially inducing generalization gaps. Such factors directly contribute to experimental variability and reproducibility concerns. Bouthillier et al. [78] showed that data sampling, initialization, and hyperparameter choices strongly influence benchmark conclusions, while Jordan et al. [79] reported concrete pathways through which training variance undermines setting comparisons and reproducibility.

More recently, tools and theories have been introduced to standardize the computation and visualization of interaction attributions. Muschalik et al. [80] released a toolkit supporting exact computation and analysis of various Shapley interaction indices, while Tsai et al. [81] proposed a faithful alternative that addresses limitations of existing interaction indices.

2.5 Interaction Effects and Higher-order Decomposition

Model performance and generalization depend not only on the main effects of individual factors but also strongly on their interactions. Friedman and Popescu [82] introduced the H-statistic to quantify non-additivity in predictive functions, establishing a standard measure of interaction strength. Lou et al. [83] demonstrated that augmenting additive models with selected two-factor terms can achieve both accuracy and interpretability. Chipman et al. [84] proposed Bayesian additive regression trees (BART) as a flexible method to absorb non-additive structures, capturing interactions effectively.

The theoretical foundations of interaction interpretation were established through functional ANOVA decomposition and variance-based sensitivity analysis. Sobol [85] introduced indices for variance allocation by order under independent inputs, while Saltelli et al. [86] systematized total sensitivity indices and estimation designs. Oakley and O’Hagan [87] formalized Bayesian surrogate-based sensitivity analysis, linking uncertainty propagation with interaction interpretation. Owen [88] analyzed Monte Carlo methods that improve estimation of small interaction indices, and Janon et al. [89] studied asymptotic properties of estimators along with variance reduction techniques. Chastaing et al. [90] extended the decomposition to dependent inputs, broadening the definition of interactions under realistic distributions.

In kernel and Gaussian process contexts, structured modeling of low-order interactions has also been explored. Durrande et al. [91] proposed ANOVA kernels, constructing reproducing kernel Hilbert spaces that enable normalization and interpretability of low-order terms. Such surrogate-based approaches lead to practical procedures for jointly estimating the magnitude and uncertainty of interaction effects.

The Shapley family provides axiomatic tools for allocating interactions. Sundararajan et al. [47] combined Shapley values with Taylor expansions to define interaction indices by order, while Lundberg et al. [45] developed efficient algorithms to compute interaction values in tree ensembles and to aggregate local explanations into global structures. This line of work provides a consistent basis for comparing the sign and magnitude of interactions at the factor-pair level.

Techniques for detecting and selecting interactions in large-scale learners have also advanced. Sorokina et al. [92] formalized ensemble-based interaction detection. Tsang, Cheng, and Liu [93] proposed an algorithm for directly identifying statistical interactions from neural network weight structures. Bien et al. [94] introduced hierarchical penalties that enforce heredity constraints, enabling interpretable interaction selection. Hooker [95] proposed generalized functional decompositions for black-box functions, offering diagnostic tools that can be integrated with experimental design.

2.6 Optimization-integrated Interpretability and Operational Decision-making

To link explanations with decision-making, attribution signals must be transformed into objective functions and constraints, and integrated into search procedures. In this context, Bayesian optimization and resource-allocation-based search have become standard tools for turning explanations into actions. Jones et al. [26] established surrogate-based global search centered on expected improvement. Shahriari et al. [27] provided a comprehensive survey of design choices and automation in machine learning settings. Snoek et al. [28] demonstrated that combining Gaussian processes with acquisition functions yields practical performance improvements across diverse models. Gardner et al. [96] introduced methods for directly handling inequality constraints, allowing safety and policy restrictions to be embedded into the design stage. Swersky et al. [97] improved search efficiency by transferring knowledge across related tasks, while Kandasamy et al. [34] combined evaluations of varying fidelities to balance cost and accuracy. Klein et al. [33] accelerated search in large-scale settings by treating dataset size as a controllable variable.

In resource-constrained environments, early stopping and bandwidth allocation become central. Li et al. [31] generalized successive halving into Hyperband, enabling rapid and distributed allocation, while Falkner et al. [32] combined Hyperband with Bayesian optimization to ensure robust performance even at scale. From a platform perspective, Feurer et al. [98] integrated preprocessing and model hyperparameter selection into unified pipelines, and Golovin et al. [35] released a service-oriented platform for large-scale experimental design execution and analysis.

When the search space extends to model architectures, optimization converges with design selection into decision-making. Zoph and Le [99] introduced reinforcement learning-based procedures for neural architecture search, while Liu et al. [100] enabled gradient-based search through continuous relaxations. Real et al. [101] demonstrated stable structure search via evolutionary strategies. These approaches align with the perspective of our study by transforming key design signals into objective functions that yield operationally viable configurations.

Safe exploration under operational constraints is also critical. Sui et al. [102] proposed a procedure that ensures compliance with safety constraints while improving efficiently, expanding applicability to risk-sensitive environments. Explicit modeling of constraints and costs matches the accountability demanded in industrial practice.

Another axis of connecting explanation signals to actionable decisions lies in counterfactual and recourse optimization. Wachter et al. [103] formulated counterfactual explanations as optimization problems that minimize changes required to achieve target outcomes. Ustun et al. [104] designed actionable recourse by incorporating cost and feasibility considerations. Mothilal et al. [105] proposed search methods for solution sets satisfying diversity and proximity, while Karimi et al. [106] systematized feasibility conditions and constraints theoretically. This line of work shifts explanations from static reports to prescriptive recommendations directly linked to changes in decision variables, naturally integrating with optimization.

3 Notation and Preliminaries

Table 1 summarizes the core symbols used throughout the main text and appendices. Unless otherwise specified, probability and expectation are interpreted with respect to the reference distribution P .

Common assumptions The model output is assumed to be bounded, and all levels and level pairs have strictly positive probabilities. Effect terms follow baseline centering: main effects are defined to have weighted mean zero, and interaction effects are defined so that their conditional means over rows and columns vanish. Independence (product distribution) assumptions are invoked only to derive simplified results for Shapley values and functional decompositions; otherwise, we retain general reference distributions in our analysis.

4 Methodology

This section presents the procedure for decomposing and estimating model outputs from the perspective of factors, defining an objective function based on two-factor approximation, and deriving optimal configurations using a lightweight search routine. Formal definitions and properties are given in §5.

4.1 Main-effect and Interaction Plots: Definition and Estimation

Let the number of factors be d , and denote the level set of each factor j by \mathcal{L}_j . The configuration space is $\mathcal{X} = \prod_{j=1}^d \mathcal{L}_j$. The reference distribution P is fixed as either a balanced or empirical reference. Given samples $\{x^{(i)}\}_{i=1}^n$ and predictions

Table 1: Symbols and abbreviations. Definitions of the main symbols used throughout the paper.

Symbol	Description	Symbol	Description
d	Number of factors	\mathcal{L}_j, L_j	Set of levels and number of levels
\mathcal{X}	Configuration space	X, x	Random configuration and fixed configuration
P	Reference distribution	$\pi_j(\ell)$	Marginal probability
$\pi_{jk}(\ell, m)$	Joint probability	$\pi_{k j}(m \ell)$	Conditional probability
f	Model output	μ, B	Baseline value and bounded constant
$g_j(\ell)$	Main effect	$g_{jk}(\ell, m)$	Interaction effect
$r(x)$	Higher-order residual	$f(x)$	Two-factor approximation
\hat{g}_j, \hat{g}_{jk}	Estimated effects	$\tilde{g}_j, \tilde{g}_{jk}$	Shrinkage-adjusted estimates
$\eta_j(\ell)$	Shrinkage coefficient for main effect	$\eta_{jk}(\ell, m)$	Shrinkage coefficient for interaction
$\hat{\mu}$	Estimate of baseline	$\{x^{(i)}\}_{i=1}^n$	Observed or evaluated configurations
$f^{(i)}$	Sampled prediction	w_i, α_i	Observation weight and normalized weight
$n_j(\ell)$	Support size of level	$n_{jk}(\ell, m)$	Support size of level pairs
n_{eff}	Effective sample size	γ_{jk}	Penalty adjustment constant
$J(x)$	Objective function	$\mathcal{R}(x)$	Uncertainty penalty
$r_{jk}(\ell, m)$	Penalty component	$C(x)$	Cost and constraint function
$\lambda_{\text{risk}}, \lambda_{\text{cost}}$	Weights for penalty and cost	$\Delta C_j(\ell)$	Cost change of level substitution
Ω	Feasible configuration set	x^*	Optimal configuration
$\phi_j(x)$	Shapley attribution	$\Delta_j(x; \pi)$	Permutation-based marginal contribution
$\hat{\phi}_j^{\text{MC}}(x)$	Monte Carlo estimate of Shapley value	\mathcal{E}	Set of evaluation points
A	Effect recovery design matrix	θ	Vector of main and pairwise effects
$\sigma_{\min}(A)$	Minimum singular value of design matrix	$\varepsilon(x)$	Error term of effects
δ	Failure probability parameter	$\ \cdot\ _{\infty}, \ \cdot\ _2$	Max norm and Euclidean norm
$d_{\text{H}}(x, y)$	Hamming distance	$\text{PCI}_{jk}(\ell, m)$	Pairwise Complementarity Index
s_{jk}	Normalization constant for PCI		

$f^{(i)}$, with nonnegative weights $w_i \geq 0$, define

$$\hat{\mu} = \frac{\sum_i w_i f^{(i)}}{\sum_i w_i}.$$

The conditional mean estimator for factor j at level ℓ is

$$\hat{\mathbb{E}}[f | X_j = \ell] = \frac{\sum_i w_i \mathbf{1}\{x_j^{(i)} = \ell\} f^{(i)}}{\sum_i w_i \mathbf{1}\{x_j^{(i)} = \ell\}}.$$

For two factors j, k at levels ℓ, m ,

$$\hat{\mathbb{E}}[f | X_j = \ell, X_k = m] = \frac{\sum_i w_i \mathbf{1}\{x_j^{(i)} = \ell, x_k^{(i)} = m\} f^{(i)}}{\sum_i w_i \mathbf{1}\{x_j^{(i)} = \ell, x_k^{(i)} = m\}}.$$

The estimators of main effects and two-factor interactions are

$$\hat{g}_j(\ell) = \hat{\mathbb{E}}[f | X_j = \ell] - \hat{\mu}, \quad \hat{g}_{jk}(\ell, m) = \hat{\mathbb{E}}[f | X_j = \ell, X_k = m] - \hat{\mathbb{E}}[f | X_j = \ell] - \hat{\mathbb{E}}[f | X_k = m] + \hat{\mu}.$$

For identifiability, we apply centering such that the weighted mean of each factor's effect is zero. For interactions, double centering is applied across rows and columns.

For levels and level pairs with weak support, shrinkage is applied. Let $n_j(\ell)$ and $n_{jk}(\ell, m)$ denote the support sizes for level ℓ and pair (ℓ, m) , respectively. Define

$$\tilde{g}_j(\ell) = \eta_j(\ell) \hat{g}_j(\ell), \quad \eta_j(\ell) = \frac{n_j(\ell)}{n_j(\ell) + \tau_j}, \quad \tilde{g}_{jk}(\ell, m) = \eta_{jk}(\ell, m) \hat{g}_{jk}(\ell, m), \quad \eta_{jk}(\ell, m) = \frac{n_{jk}(\ell, m)}{n_{jk}(\ell, m) + \tau_{jk}},$$

where $\tau_j, \tau_{jk} > 0$ are shrinkage strengths. Uncertainty is quantified via bootstrap estimates of standard errors and confidence intervals.

SHAP-based estimation option Fix an evaluation set \mathcal{E} , and at each $x \in \mathcal{E}$, compute the Shapley contribution $\hat{\phi}_j^{\text{MC}}(x)$ for factor j using Monte Carlo. Under an independent reference distribution, the two-factor relationship

$$\phi_j(x) = g_j(x_j) + \frac{1}{2} \sum_{k \neq j} g_{jk}(x_j, x_k)$$

is treated as a linear constraint, leading to the least-squares problem

$$\min_{\{g_j, g_{jk}\}} \sum_{x \in \mathcal{E}} \sum_{j=1}^d \left(\hat{\phi}_j^{\text{MC}}(x) - g_j(x_j) - \frac{1}{2} \sum_{k \neq j} g_{jk}(x_j, x_k) \right)^2.$$

Centering constraints are given by $\sum_{\ell} \pi_j(\ell) g_j(\ell) = 0$ and $\sum_m \pi_{k|j}(m | \ell) g_{jk}(\ell, m) = 0$. Denote the solution as \hat{g}_j, \hat{g}_{jk} , and apply the same shrinkage procedure $\tilde{g}_j = \eta_j \hat{g}_j, \tilde{g}_{jk} = \eta_{jk} \hat{g}_{jk}$. Confidence intervals are obtained by combining variance estimates of $\hat{\phi}_j^{\text{MC}}(x)$ at each evaluation point with bootstrap resampling.

4.2 Two-factor Approximation and Objective Function

This subsection defines the two-factor approximation and objective function using the effect estimates obtained previously. The two-factor approximation is expressed as the sum of main effects and pairwise interactions. We consider two estimation paths. The first is the Cell-mean (CM) path, which fills effect tables directly with conditional means of design cells. The second is the SHAP-fit (SF) path, which aggregates SHAP contributions across configurations and fits effect tables via least squares under centering constraints. Subsequent steps—including the approximation function, objective function, penalties for risk and cost, and the solver—are identical across the two paths.

The two-factor approximation is defined as

$$\tilde{f}(x) = \hat{\mu} + \sum_{j=1}^d \tilde{g}_j(x_j) + \sum_{1 \leq j < k \leq d} \tilde{g}_{jk}(x_j, x_k).$$

The objective function for a configuration x is

$$J(x) = \tilde{f}(x) - \lambda_{\text{risk}} \mathcal{R}(x) - \lambda_{\text{cost}} C(x),$$

where $C(x)$ quantifies implementation costs and domain constraints. Infeasible configurations are excluded from the feasible search set $\Omega \subseteq \mathcal{X}$. The uncertainty penalty is defined in terms of support information as

$$\mathcal{R}(x) = \sum_{1 \leq j < k \leq d} r_{jk}(x_j, x_k), \quad r_{jk}(\ell, m) = \frac{\gamma_{jk}}{n_{jk}(\ell, m) + \gamma_{jk}},$$

where $\gamma_{jk} > 0$ is an adjustment constant and $n_{jk}(\ell, m)$ denotes the support size of level pair (ℓ, m) .

4.3 Optimal Configuration Solver

The goal is to maximize the objective function $J(x)$ over the feasible set Ω . We adopt a coordinate ascent–based search procedure as the default solver. The initial configuration is constructed by selecting the top levels of each factor based on main effects. Thereafter, one factor is updated at a time by replacing it with the level that yields the greatest increase in $J(x)$. The process stops when a full sweep across all factors results in no further improvement. To enhance robustness, multiple restarts and beam search with top-level restrictions are employed. The operational steps of the solver are summarized in Algorithm 1.

Here, $\Delta C_j(\ell)$ denotes the change in cost when factor j is switched to level ℓ . The complexity of one coordinate sweep is approximately $O(d^2 L)$, where L is the average number of levels per factor. Because the search space is finite, monotonic improvement and termination are guaranteed. Further properties are established in §5.

5 Theoretical Foundations

This section presents the formal definitions and justifications of our methodology. Notation follows the unified symbols in §3.

Algorithm 1: Optimal Configuration Solver**Input:** Effects $\tilde{g}_j, \tilde{g}_{jk}$; penalties r_{jk} ; cost C ; weights $\lambda_{\text{risk}}, \lambda_{\text{cost}}$; feasible set Ω ; initial configuration set \mathcal{S}_0 **Output:** $x^* \in \Omega$ **for** $x \in \mathcal{S}_0$ **do** $\Delta J \leftarrow \infty$ **repeat** $x_{\text{prev}} \leftarrow x$ **for** $j = 1$ **to** d **do** $x_j \leftarrow \arg \max_{\ell \in \mathcal{L}_j, (x_{-j}, \ell) \in \Omega} \tilde{g}_j(\ell) + \sum_{k \neq j} \tilde{g}_{jk}(\ell, x_k) - \lambda_{\text{risk}} \sum_{k \neq j} r_{jk}(\ell, x_k) - \lambda_{\text{cost}} \Delta C_j(\ell)$ $\Delta J \leftarrow J(x) - J(x_{\text{prev}})$ **until** $\Delta J < \varepsilon$ $\mathcal{S} \leftarrow \mathcal{S} \cup \{x\}$ **return** $\arg \max_{x \in \mathcal{S}} J(x)$

5.1 Assumptions and Formulation

Definition 5.1 (Design space and reference distribution). Let the number of factors be d , and denote the set of levels for factor j by \mathcal{L}_j . The configuration space is $\mathcal{X} = \prod_{j=1}^d \mathcal{L}_j$. The reference distribution P is fixed as a probability distribution over \mathcal{X} , and the baseline value is defined as $\mu := \mathbb{E}_{X \sim P}[f(X)]$.

Definition 5.2 (Centering constraints). For each factor j and level $\ell \in \mathcal{L}_j$, the main effect $g_j(\ell)$ is defined such that its expectation with respect to the marginal distribution of P is zero. For any distinct factors $j \neq k$ and level pair (ℓ, m) , the interaction $g_{jk}(\ell, m)$ is defined such that its row and column averages vanish under the conditional distribution of P .

Throughout this subsection, we assume that the model output is bounded and that every level and level pair has strictly positive probability. That is, $|f(x)| \leq B$ and $P(X_j = \ell) > 0$, $P(X_j = \ell, X_k = m) > 0$.

Proposition 5.3 (Existence and uniqueness of functional decomposition). *In the Hilbert space with inner product $\langle u, v \rangle = \mathbb{E}_P[uv]$, the function f admits the unique decomposition*

$$f(x) = \mu + \sum_{j=1}^d g_j(x_j) + \sum_{1 \leq j < k \leq d} g_{jk}(x_j, x_k) + r(x),$$

where r represents higher-order (≥ 3) interaction components and is orthogonal to the subspaces defined by the centering constraints above.

Proof sketch. The result follows from projections onto conditional expectation subspaces and orthogonal complements. Main effects correspond to projections onto univariate subspaces, and interactions correspond to projections onto bivariate subspaces with the main-effect subspaces removed. Orthogonal decomposition in Hilbert spaces ensures uniqueness. \square

5.2 Shapley Contributions and Approximation

Definition 5.4 (Shapley contributions and two-factor decomposition). Consider the Shapley contribution $\phi_j(x)$ defined with respect to the background distribution P . If f admits the decomposition in Proposition 5.3, then the Shapley contribution can itself be decomposed as follows.

Theorem 5.5 (Two-factor decomposition of Shapley contributions). *Suppose the decomposition in Proposition 5.3 holds and P is a product distribution with independent factors. Then, for every $x \in \mathcal{X}$ and every j ,*

$$\phi_j(x) = g_j(x_j) + \frac{1}{2} \sum_{k \neq j} g_{jk}(x_j, x_k).$$

Moreover, the efficiency property holds: $\sum_{j=1}^d \phi_j(x) = f(x) - \mu$.

Proof sketch. Apply the symmetry and dummy axioms of Shapley values. Since g_j depends only on factor j , its entire contribution is attributed to j . For interaction terms g_{jk} , the effect is shared equally between the two factors j and k . The sum matches $f(x) - \mu$ by the efficiency property. \square

Corollary 5.6 (Consistency of the two-factor approximation). *The two-factor approximation*

$$\tilde{f}(x) = \mu + \sum_j g_j(x_j) + \sum_{j < k} g_{jk}(x_j, x_k)$$

can be equivalently expressed as the sum of Shapley contributions by Theorem 5.5.

Remark 5.7 (Centering and efficiency of estimates). When practical estimates \hat{g}_j, \hat{g}_{jk} are centered according to the constraints, the resulting Shapley sums also satisfy efficiency. This ensures that the objective function remains invariant to baseline shifts.

5.3 Error Decomposition and Sample Complexity

This subsection separates estimation error from approximation error and provides sample size requirements.

Definition 5.8 (Error terms). The estimates $\tilde{g}_j, \tilde{g}_{jk}$ are shrinkage- and centering-adjusted. The two-factor approximation error is denoted by $r(x)$, while the estimation error is defined as

$$\varepsilon(x) := \sum_j (\tilde{g}_j(x_j) - g_j(x_j)) + \sum_{j < k} (\tilde{g}_{jk}(x_j, x_k) - g_{jk}(x_j, x_k)).$$

Theorem 5.9 (Error decomposition of expected performance). *For every x ,*

$$\tilde{f}(x) - f(x) = \varepsilon(x) - r(x).$$

Moreover, under the mean-squared criterion,

$$\mathbb{E}_P[(\tilde{f} - f)^2] \leq 2\mathbb{E}_P[\varepsilon^2] + 2\mathbb{E}_P[r^2].$$

Proof sketch. The identity follows directly from the definitions. The inequality is obtained via the parallelogram (or Pythagorean-type) inequality, here applied as Pearson's inequality. \square

Theorem 5.10 (Concentration of cell means and sample complexity). *Suppose f is bounded within $[-B, B]$. Let $n_{jk}(\ell, m)$ denote the cell size for level pair (ℓ, m) . In unweighted simple mean estimation, for any $\delta \in (0, 1)$,*

$$\Pr\left(\left|\widehat{\mathbb{E}}[f \mid X_j = \ell, X_k = m] - \mathbb{E}[f \mid X_j = \ell, X_k = m]\right| \leq B\sqrt{\frac{2\log(2/\delta)}{n_{jk}(\ell, m)}}\right) \geq 1 - \delta.$$

Hence, a sufficient condition for ensuring that the mean error of each cell is at most ϵ is

$$n_{jk}(\ell, m) \geq 2B^2\epsilon^{-2}\log(2/\delta).$$

Proof sketch. Apply Hoeffding's inequality to the sample average within each cell. \square

Corollary 5.11 (Uniform convergence of the two-factor approximation). *Let n_{\min} denote the minimum cell size over the finite set of cells. Then, with probability at least $1 - \delta$, all cell mean errors are bounded on the order of $O(\sqrt{\log(1/\delta)/n_{\min}})$, and the uniform error of \tilde{f} converges at the same rate.*

Remark 5.12 (Role of shrinkage). Shrinkage reduces the variance of terms with small cell sizes, thereby decreasing $\mathbb{E}[\varepsilon^2]$. Although it increases bias, the total error is minimized at an appropriate shrinkage strength.

5.4 Optimality Gap

The objective function is defined as

$$J(x) = \tilde{f}(x) - \lambda_{\text{risk}}\mathcal{R}(x) - \lambda_{\text{cost}}C(x),$$

which can be expressed as the sum of univariate and bivariate terms.

Lemma 5.13 (Monotonic improvement and finite termination). *Each coordinate update step does not decrease J . Since the configuration space is finite, the algorithm terminates in a finite number of steps.*

Proof sketch. At each step, the level of one coordinate is updated to maximize J , ensuring non-decreasing value. In a finite space, revisiting the same configuration implies termination. \square

Definition 5.14 (1-swap optimality). A configuration \hat{x} is 1-swap optimal if changing any single factor to another level does not increase J .

Proposition 5.15 (Termination point of coordinate ascent is 1-swap optimal). *When the procedure in Lemma 5.13 terminates, the resulting solution is 1-swap optimal.*

Proof sketch. At termination, no single-coordinate change yields a larger J . By definition, the solution is 1-swap optimal. \square

Theorem 5.16 (Global optimality under diagonal dominance). *For each factor j , let m_j denote the minimum main-effect gain margin, and let L_{jk} be an upper bound on the variation due to interactions between factor j and any other factor k . If for all j ,*

$$\sum_{k \neq j} L_{jk} < m_j,$$

then J exhibits coordinate-wise contraction properties, and every 1-swap optimal solution is globally optimal. Moreover, the termination point is unique.

Proof sketch. If the best response in one coordinate is Lipschitz continuous with respect to changes in others, and the self-contribution dominates the sum of cross-interactions, then the best-response operator is a contraction mapping. By Banach’s fixed point theorem, a unique fixed point exists, which is the global optimum. \square

Remark 5.17 (Structural conditions and stronger guarantees). If the interaction matrix has attractive structure or satisfies submodularity constraints, global optimality can also be achieved via cut-based or dynamic programming methods. In such cases, coordinate ascent provides a useful warm start for faster convergence.

5.5 Properties and Interpretation of PCI

Definition 5.18 (PCI: Pairwise Complementarity Index). For a factor pair (j, k) and level pair (ℓ, m) , define

$$\text{PCI}_{jk}(\ell, m) := \frac{g_{jk}(\ell, m)}{s_{jk}}, \quad s_{jk} := \left(\frac{1}{|\mathcal{L}_j||\mathcal{L}_k|} \sum_{\ell', m'} g_{jk}(\ell', m')^2 \right)^{1/2}.$$

Here, s_{jk} is the root-mean-square strength of the interaction.

Proposition 5.19 (Centering and scale invariance). *For every row and column, the weighted mean of PCI is zero. Moreover, PCI is invariant under affine transformations of f : if $f \mapsto af + b$ with $a > 0$, then PCI remains unchanged.*

Proof sketch. By double-centering of g_{jk} , row and column averages vanish. Both numerator and denominator scale proportionally under affine transformations, leaving the ratio unchanged. \square

Proposition 5.20 (Comparability). *Within a given factor pair, the ranking of PCI values is identical to that of g_{jk} . Across different factor pairs, PCI removes scale differences, allowing relative strength of interactions to be compared.*

Proof sketch. For the same factor pair, the denominator is constant, so rankings are preserved. When comparing across pairs, standardization by s_{jk} eliminates scale disparities. \square

Remark 5.21 (Connection to the objective function). In the objective function, the contribution of interaction terms is computed directly via g_{jk} . PCI serves as a dimensionless summary for reporting and diagnostics, while practical selection decisions are made using the original g_{jk} together with cost and risk penalties.

5.6 Monte Carlo Approximation: Consistency and Sample Complexity

Definition 5.22 (Monte Carlo Shapley estimator). For an evaluation point x and factor j , let a single marginal contribution be $\Delta_j(x; S)$. The Monte Carlo estimator with M samples is

$$\hat{\phi}_j^{\text{MC}}(x) = \frac{1}{M} \sum_{s=1}^M \Delta_j(x; S_s),$$

where S_s is drawn from either a uniform permutation or a uniform subset distribution.

Throughout this subsection, we assume the model output is bounded and all levels and level pairs have positive probability: $|f(x)| \leq B$, $P(X_j = \ell) > 0$, and $P(X_j = \ell, X_k = m) > 0$.

Lemma 5.23 (Boundedness of marginal contributions). *For all x and j , $|\Delta_j(x; S)| \leq 2B$.*

Proof sketch. Each marginal contribution is the difference of two conditional expectations, each in $[-B, B]$, so the absolute difference is at most $2B$. \square

Theorem 5.24 (Concentration for a single coordinate). *For any x and j , with probability at least $1 - \delta$,*

$$|\hat{\phi}_j^{\text{MC}}(x) - \phi_j(x)| \leq 2B \sqrt{\frac{2 \log(2/\delta)}{M}}.$$

Thus, to achieve tolerance ε , it suffices to take $M \geq 8B^2 \varepsilon^{-2} \log(2/\delta)$.

Proof sketch. Apply Hoeffding's inequality using the bound from Lemma 5.23. \square

Corollary 5.25 (Uniform bound across multiple coordinates and evaluation points). *For an evaluation set \mathcal{E} and d factors, with probability at least $1 - \delta$, for all $x \in \mathcal{E}$ and all j ,*

$$|\hat{\phi}_j^{\text{MC}}(x) - \phi_j(x)| \leq 2B \sqrt{\frac{2 \log(2d|\mathcal{E}|/\delta)}{M}}.$$

Remark 5.26 (Variance-adaptive refinement). A Bernstein-type bound gives

$$|\hat{\phi}_j^{\text{MC}}(x) - \phi_j(x)| \leq \sqrt{\frac{2\hat{\sigma}^2 \log(3/\delta)}{M}} + \frac{6B \log(3/\delta)}{M},$$

where $\hat{\sigma}^2$ is the empirical variance of the marginal contributions.

Proposition 5.27 (Propagation error to FACTORS effect tables). *Under the independence product assumption of Theorem 5.5,*

$$\phi_j(x) = g_j(x_j) + \frac{1}{2} \sum_{k \neq j} g_{jk}(x_j, x_k).$$

Suppose g_j and g_{jk} are recovered by least squares. If the Monte Carlo error satisfies $\max_{x \in \mathcal{E}, j} |\hat{\phi}_j^{\text{MC}}(x) - \phi_j(x)| \leq \eta$, then under finite condition number of the design matrix, there exists a constant $C_{\mathcal{E}}$ such that

$$|\hat{g}_j - \tilde{g}_j| \leq C_{\mathcal{E}} \eta, \quad |\hat{g}_{jk} - \tilde{g}_{jk}| \leq C_{\mathcal{E}} \eta$$

for all levels and level pairs.

Proof sketch. This follows from the stability of linear systems: under bounded condition number, solution error is linearly proportional to observation error. \square

Theorem 5.28 (Deviation bound for the objective function). *In the above setting, if risk and cost terms do not depend on Monte Carlo estimates, then for all x ,*

$$|\hat{J}(x) - J(x)| \leq \sum_j |\hat{g}_j(x_j) - \tilde{g}_j(x_j)| + \sum_{j < k} |\hat{g}_{jk}(x_j, x_k) - \tilde{g}_{jk}(x_j, x_k)|.$$

Combining Corollary 5.25 with Proposition 5.27, there exists a constant C such that

$$\sup_{x \in \Omega} |\hat{J}(x) - J(x)| \leq C \sqrt{\frac{\log(2d|\mathcal{E}|/\delta)}{M}}.$$

Proof sketch. By definition, J differs from \hat{J} only through the effect terms. Substituting the uniform error bound and linear stability yields the result. \square

Remark 5.29 (Practical rule for choosing sample size). Treating the total number of items as $d|\mathcal{E}|$, for target error ε and confidence δ , a sufficient choice is

$$M \asymp B^2 \varepsilon^{-2} \log(d|\mathcal{E}|/\delta).$$

Between cell-average error and Monte Carlo error, the larger one dominates; thus, M should be chosen near the balance point of the two.

6 Experimental Design

We present three experiments that illustrate how FACTORS approximates the performance function using main effects and two-factor interactions, then selects optimal configurations via a risk- and cost-adjusted objective function. All experiments follow the unified notation and terminology.

6.1 Simulation Study

Objective To verify whether the approximation map constructed from main effects and two-factor interactions captures the core structure of the performance function. We also assess whether the CM and SF paths produce consistent estimates, and whether the optimality gap decreases as the number of design points increases.

Design The number of factors is set between six and eight, each with two or three discrete levels. The teacher function explicitly incorporates main effects and two-factor interactions, with small higher-order residual terms added. Two sets of design points are prepared for comparison: a balanced design and a distributional design reflecting realistic sampling.

Procedure At each design point, the teacher function is evaluated to collect performance samples. In the CM path, main effects and interactions are estimated via conditional means with shrinkage applied to sparse cells. In the SF path, factor Shapley values are estimated and then reconstructed via least squares using the relation

$$\phi_j(x) = g_j(x_j) + \frac{1}{2} \sum_{k \neq j} g_{jk}(x_j, x_k).$$

Stability of reconstruction is diagnosed via the minimum singular value of the design matrix and residual magnitudes. The approximation map \tilde{f} is then used to define the objective function

$$J(x) = \tilde{f}(x) - \lambda_{\text{risk}} R(x) - \lambda_{\text{cost}} C(x),$$

and candidate solutions are obtained using coordinate ascent with multiple restarts.

Evaluation Metrics We report the optimality gap of the objective function, sign and rank consistency of top effects, confidence interval widths, design matrix conditioning, and distribution of cell supports. Success criteria are consistency between CM and SF effect estimates, monotonic decline of the optimality gap, and qualitative confirmation that risk penalties suppress sparse configurations.

6.2 Benchmark Dataset Experiments

Objective To verify that FACTORS can construct stable performance maps of the configuration space in realistic training pipelines and recommend optimal configurations that account for both risk and cost. Beyond exhaustive search or single-shot comparisons, we assess whether the method provides actionable recommendations with explicit justification for operational decision-making.

Design We adopt benchmarks spanning regression, categorical tabular classification, and image classification: UCI Concrete, UCI Car Evaluation, and Fashion-MNIST. Concrete involves regression on compressive strength using standardized continuous features. Car Evaluation consists entirely of categorical features and is handled as multiclass classification with one-hot encoding. FMNIST uses 28×28 grayscale images from 10 classes. For UCI Concrete and Car Evaluation, we employ lightweight MLPs; for FMNIST, we use a shallow convolutional neural network. For regression tasks, the same MLP backbone is coupled with a regression loss. Factors are defined uniformly as operational hyperparameters: optimizer (Adam vs. momentum SGD), learning rate (low, medium, high buckets), batch size (64, 128, 256), weight decay (10^{-4} , 5×10^{-4} , 10^{-3}), and number of epochs (10, 20, 30). Infeasible or unreasonable combinations are excluded in advance. The grid is aligned across tasks with the same factor definitions, and between 60 and 120 design points are sampled in a balanced manner according to budget constraints.

Procedure For each design point, performance is collected under a common training and evaluation protocol. Two parallel paths are then used to construct effect tables: the first estimates main effects and two-factor interactions directly from observed means, while the second computes SHAP contributions and recovers the same-order effect table via least squares. Both paths apply mild Tikhonov shrinkage to mitigate uncertainty in sparse cells. The default background distribution is uniform (consistent with DOE assumptions), with empirical frequency backgrounds compared as a robustness check. Sensitivity to sample budget is studied by gradually increasing the number of seeds, and robustness to partial designs is assessed by comparing balanced versus biased samples. Once an approximation map is obtained, the objective function incorporating risk and cost is computed. Promising configurations are identified via coordinate ascent combined with restricted beam search, retrained, and evaluated on independent validation sets for performance

and constraint satisfaction. Evaluation uses RMSE for regression and accuracy for classification, with macro-averaged metrics cross-checked for class imbalance in Car Evaluation.

Evaluation Metrics We record the objective function value, optimality gap, constraint satisfaction rate, runtime, and resource usage. Effect map quality is summarized by consistency of top main effects and two-factor interactions as well as confidence interval widths. Success criteria are improvement of the objective function under proposed configurations, satisfaction of constraints, consistency between CM and SF effect estimates, and rising rank stability with more seeds. Final validation checks whether balanced designs yield more consistent maps than biased ones. Across all three benchmarks, the goal is to demonstrate that FACTORS supports hyperparameter selection in practical settings with stability and cost efficiency.

6.3 Ablation Study

Objective To disentangle the impact of individual pipeline components on performance and stability, and thereby explain the underlying mechanisms.

Axes of Variation The following axes are considered: choice of estimation path, magnitude of shrinkage strength, values of risk and cost weights, initialization and beam width and sweep order of the optimizer, and design point composition including the form of the background distribution.

Protocol One axis is varied at a time while all other conditions remain fixed. For each configuration, we record changes in confidence intervals and residuals of the effect table, condition numbers of the design matrix, objective values and optimality gaps, as well as runtime. Pairs of axes with strong interactions are additionally cross-checked.

Evaluation Criteria For shrinkage strength, thresholds of over-shrinkage and under-shrinkage should emerge. Increasing the risk weight should suppress selection of sparse configurations and reduce variability in the objective function. Enlarging the design set should narrow confidence intervals of effect estimates and decrease the optimality gap. Optimizer hyperparameters should exhibit a consistent trade-off between runtime and objective improvement.

7 Experiments

7.1 Simulation Results

The results of the simulation experiments are as follows. In balanced designs with mixed levels, the SF path consistently outperformed CM across all metrics, including effect table reconstruction, policy optimization, and rank preservation. Decomposing Shapley contributions into main and interaction effects and then recovering them via least squares reduced interaction leakage, substantially lowering reconstruction error. Consequently, the optimal configuration obtained by maximizing the estimated objective function matched the true optimum, driving the optimality gap effectively to zero. Detailed results are reported in Table 2.

Table 2: Simulation results. The table reports means and 95% confidence intervals. Reconstruction error measures the difference between estimated and true effect tables, while optimality gap reflects the performance gap of the policy derived from the estimated table relative to the true optimum. ρ denotes the Spearman rank correlation between estimated and true policy scores.

Method	Reconstruction error		Optimality gap		ρ	
	mean	95% CI	mean	95% CI	mean	95% CI
CM	0.1479	[0.1468, 0.1490]	0.4736	[-0.0252, 0.9725]	0.9014	[0.9005, 0.9023]
SF	0.0622	[0.0615, 0.0628]	0.0000	[0.0000, 0.0000]	0.9323	[0.9316, 0.9331]

7.2 Benchmark Results

7.2.1 UCI Concrete

The UCI Concrete results show that even main effects alone provide a clear signal for policy decisions. As summarized in Table 3, the learning-rate factor has the strongest impact, with mean objective values differing significantly across high, medium, and low levels. The 95% confidence intervals of the three levels do not overlap, confirming a statistically clear separation. Optimizer choice also matters, with Adam consistently outperforming SGD. For batch size, 64 yields better results than 256, and for epochs, 150 is consistently superior to 50. In contrast, L_2 regularization has negligible influence, with values at 0 and 0.001 producing nearly identical effects.

Table 4 reinforces these findings. The top two configurations both use Adam, high learning rate, batch size 64, and 150 epochs, with performance indistinguishable between $L_2 = 0$ and $L_2 = 0.001$ within confidence intervals. Increasing the batch size to 256 within the same core combination keeps the configuration in the upper ranks, but with a statistically significant drop relative to the top tier. An SGD variant with high learning rate, batch size 64, and 150 epochs also appears near the lower end of the top ten but still falls well behind the Adam-based setups.

In summary, the learning rate emerges as the most decisive factor, followed by optimizer, batch size, and epochs, while L_2 regularization remains inconsequential. This structure aligns with FACTORS’ approximation assumptions and suggests that in practice, a baseline policy should adopt Adam with a high learning rate, batch size 64, and 150 epochs, with batch size and epochs subsequently fine-tuned according to resource and constraint considerations.

Table 3: Main effects for the UCI Concrete dataset. Means are computed across all rows and seeds; values in parentheses denote 95% confidence intervals.

Factor	Level	Mean	95% CI
Batch size	64	-8.7206	[-8.9620, -8.4791]
	256	-10.9667	[-11.2689, -10.6644]
Epochs	150	-8.7114	[-8.9591, -8.4637]
	50	-10.9758	[-11.2722, -10.6795]
Learning rate	high	-7.7583	[-7.9942, -7.5225]
	mid	-9.3441	[-9.5942, -9.0940]
	low	-12.4283	[-12.7539, -12.1027]
Optimizer	Adam	-8.5782	[-8.8479, -8.3084]
	SGD	-11.1091	[-11.3736, -10.8445]
L_2	0.0000	-9.8431	[-10.1389, -9.5473]
	0.0010	-9.8441	[-10.1398, -9.5485]

Table 4: Top 10 configurations for the UCI Concrete dataset. Values are mean scores across seeds with 95% confidence intervals.

Optimizer	Learning rate	Batch size	L_2	Epochs	Mean	95% CI
Adam	high	64	0.0000	150	-5.3295	[-5.5592, -5.0998]
Adam	high	64	0.0010	150	-5.3416	[-5.5834, -5.0998]
Adam	high	256	0.0010	150	-6.0167	[-6.2640, -5.7695]
Adam	high	256	0.0000	150	-6.0195	[-6.2737, -5.7653]
Adam	high	64	0.0000	50	-6.2700	[-6.5448, -5.9953]
Adam	high	64	0.0010	50	-6.2777	[-6.5559, -5.9994]
Adam	mid	64	0.0000	150	-6.2937	[-6.5468, -6.0407]
Adam	mid	64	0.0010	150	-6.2952	[-6.5511, -6.0393]
SGD	high	64	0.0000	150	-7.2611	[-7.5082, -7.0140]
SGD	high	64	0.0010	150	-7.2616	[-7.5087, -7.0144]

7.2.2 UCI Car Evaluation

Table 5 shows that main effects are highly pronounced. Learning rate has the strongest influence, with the high level clearly outperforming medium and low, and the 95% confidence intervals across the three levels are non-overlapping. Optimizer choice is also decisive, with Adam substantially better than SGD. Batch size 64 consistently outperforms 256, and 150 epochs is clearly superior to 50. By contrast, L_2 regularization has negligible impact, with values at 0 and 0.001 producing virtually identical effects.

Table 6 confirms these patterns at the configuration level. Top-ranked combinations all include Adam with high learning rate, batch size 64, and 150 epochs. Variations in L_2 between 0 and 0.001 do not affect rankings. Increasing the batch size to 256 or lowering the learning rate to medium reduces both the mean objective and its confidence interval. SGD-based configurations appear only at the lower end of the top ten and remain substantially behind Adam-based configurations.

In summary, learning rate is the primary determinant, followed by optimizer, batch size, and epochs, while L_2 is inconsequential. From a policy recommendation perspective, the baseline configuration should adopt Adam with high learning rate, batch size 64, and 150 epochs, with L_2 safely fixed for simplicity.

Table 5: Main effects for the UCI Car Evaluation dataset. Means are computed across all rows and seeds; values in parentheses denote 95% confidence intervals.

Factor	Level	Mean	95% CI
Batch size	64	0.8902	[0.8804, 0.8999]
	256	0.7986	[0.7865, 0.8106]
Epochs	150	0.8878	[0.8777, 0.8978]
	50	0.8009	[0.7890, 0.8129]
Learning rate	high	0.9227	[0.9123, 0.9330]
	mid	0.8632	[0.8517, 0.8747]
	low	0.7472	[0.7348, 0.7596]
Optimizer	Adam	0.9006	[0.8901, 0.9112]
	SGD	0.7881	[0.7777, 0.7985]
L_2	0.0000	0.8444	[0.8325, 0.8563]
	0.0010	0.8443	[0.8325, 0.8562]

Table 6: Top 10 configurations for the UCI Car Evaluation dataset. Values are mean scores across seeds with 95% confidence intervals.

Optimizer	Learning rate	Batch size	L_2	Epochs	Mean	95% CI
Adam	high	64	0.0000	150	0.9951	[0.9929, 0.9974]
Adam	high	64	0.0010	150	0.9951	[0.9927, 0.9975]
Adam	high	256	0.0000	150	0.9917	[0.9881, 0.9953]
Adam	high	256	0.0010	150	0.9913	[0.9877, 0.9949]
Adam	high	64	0.0000	50	0.9908	[0.9874, 0.9942]
Adam	mid	64	0.0000	150	0.9902	[0.9868, 0.9937]
Adam	high	64	0.0010	50	0.9901	[0.9866, 0.9936]
Adam	mid	64	0.0010	150	0.9901	[0.9867, 0.9935]
SGD	high	64	0.0010	150	0.9644	[0.9607, 0.9681]
SGD	high	64	0.0000	150	0.9644	[0.9607, 0.9681]

7.2.3 Fashion MNIST

Table 7 shows that the directions of main effects are clear. Optimizer choice is decisive, with Adam strongly outperforming SGD and the confidence intervals not overlapping. Epochs also play a major role, with 30 epochs consistently superior to 15. Batch size 64 performs better than 256, highlighting the advantage of smaller batches. Learning rate levels reveal that high and medium are close to each other and both clearly outperform low. L_2 regularization has negligible effect, as the two levels yield nearly identical outcomes.

Table 8 illustrates how the top front of configurations is formed. All top-ranked configurations use Adam, with 30 epochs dominating. Interestingly, the very best configuration combines medium learning rate with batch size 256, a case where interaction effects overturn the main-effect signal that favored smaller batches. Substituting batch size 64 or shifting the learning rate to low or high reduces the mean objective and its confidence interval. Within the top tier, changes in L_2 do not meaningfully alter rankings.

In summary, for FMNIST the highest priorities are optimizer and epochs, followed by batch size and learning rate, while L_2 can be safely simplified. From a policy recommendation standpoint, Adam with 30 epochs should be taken as the baseline, with medium learning rate as the preferred choice. Both batch sizes 64 and 256 should be retained as candidates, as their relative standing depends on interaction effects that require confirmation through retraining.

7.3 Ablation Results

Table 9 summarizes how theoretical predictions are reproduced across four ablation axes. The overall message is that incorporating two-factor approximations is essential for rank preservation and accurate identification of optimal configurations, and that SF reconstruction remains robust under partial and biased designs.

First, panel (a) shows that including both main effects and two-factor interactions substantially improves performance. Compared to using only main effects, where Spearman correlation is 0.7695 and the optimality gap is 0.0049, adding two-factor interactions raises the correlation to 0.9602 and reduces the gap to 0.0017. Under near-complete grids, CM and SF yield virtually identical values, confirming the consistency of least-squares reconstruction from Shapley contributions.

Table 7: Main effects for the Fashion MNIST dataset. Means are computed across all rows and seeds; values in parentheses denote 95% confidence intervals.

Factor	Level	Mean	95% CI
Batch size	64	0.8872	[0.8862, 0.8881]
	256	0.8811	[0.8796, 0.8825]
Epochs	30	0.8869	[0.8859, 0.8879]
	15	0.8813	[0.8799, 0.8827]
Learning rate	high	0.8866	[0.8855, 0.8877]
	mid	0.8851	[0.8837, 0.8864]
	low	0.8806	[0.8788, 0.8825]
Optimizer	Adam	0.8892	[0.8883, 0.8901]
	SGD	0.8790	[0.8777, 0.8803]
L_2	0.0000	0.8842	[0.8829, 0.8854]
	0.0001	0.8841	[0.8828, 0.8853]

Table 8: Top 10 configurations for the Fashion MNIST dataset. Values are mean scores across seeds with 95% confidence intervals.

Optimizer	Learning rate	Batch size	L_2	Epochs	Mean	95% CI
Adam	mid	256	0.0001	30	0.8946	[0.8908, 0.8985]
Adam	mid	256	0.0000	30	0.8941	[0.8899, 0.8983]
Adam	mid	64	0.0000	15	0.8932	[0.8899, 0.8966]
Adam	low	64	0.0001	30	0.8932	[0.8900, 0.8963]
Adam	low	64	0.0000	30	0.8931	[0.8897, 0.8965]
Adam	high	256	0.0001	30	0.8929	[0.8886, 0.8973]
Adam	mid	64	0.0001	15	0.8927	[0.8880, 0.8973]
Adam	high	256	0.0000	30	0.8913	[0.8880, 0.8946]
Adam	high	256	0.0000	15	0.8902	[0.8868, 0.8936]
Adam	low	64	0.0000	15	0.8900	[0.8857, 0.8944]

Panel (b) demonstrates robustness under partial designs. With balanced samples, SF achieves a Spearman correlation of 0.9496 and maintains an optimality gap around 0.0015. Even with skewed samples, SF retains high correlation (0.9570), indicating low sensitivity to sampling bias. In contrast, CM drops from 0.8074 to 0.6574 in correlation when moving from balanced to skewed designs. The deceptively low optimality gap (0.0005) for CM in the skewed case is explained by accidental overemphasis of particular configurations due to bias. From an operational standpoint, this highlights the importance of evaluating rank stability rather than relying solely on a single optimal value.

Panel (c) evaluates the effect of SHAP background distribution. With a uniform background, Spearman correlation is 0.9496, slightly higher than the empirical background at 0.9420. Optimality gaps remain around 0.0015 in both cases. These results justify adopting the uniform factor assumption as a default in DOE settings.

Panel (d) illustrates the seed budget curve. Spearman correlation increases steadily from 0.9368 with 2 seeds to 0.9602 with 16 seeds, showing improved stability and reproducibility of the effect maps. While optimality gap exhibits minor non-monotonic fluctuations at very low budgets, it converges at higher budgets. This matches the theoretical sample complexity analysis and provides a practical guideline: avoid overinterpreting low optimality gaps from single seeds, and instead report correlations and confidence intervals, with decision risk decreasing as the budget increases.

In sum, FACTORS maps with two-factor approximations faithfully reconstruct the global ranking structure. SF offers consistent performance even with partial or biased designs, and strategies that default to uniform backgrounds and gradually increase seed budgets are the safest. These findings align with the approximation assumptions, error decomposition, and sample complexity analysis presented in the theoretical sections.

8 Discussion

8.1 Main and Interaction Effects: Definition, Estimation, and Visualization Guide

Main-effect plots align conditional mean performance by factor levels, revealing both the direction and magnitude of changes. Across datasets, several consistent signals were observed. Optimizer choice strongly favored Adam. Learning-rate levels showed a clear monotonic trend, with higher values yielding superior performance. Smaller batch sizes

Table 9: Summary of ablation experiments: (a) effects order, (b) design robustness, (c) SHAP background, (d) seed budget. Metrics are true optimality gap and Spearman rank correlation against ground truth.

(a) Effects order				(b) Design robustness ($n = 24$)			
Scenario	Estimator	Optimality gap	Spearman	Design	Estimator	Optimality gap	Spearman
pairwise	CM	0.0017	0.9602	balanced	CM	0.0020	0.8074
pairwise	SF	0.0017	0.9602	balanced	SF	0.0015	0.9496
mains-only	CM	0.0049	0.7695	skewed	CM	0.0005	0.6574
mains-only	SF	0.0049	0.7695	skewed	SF	0.0015	0.9570

(c) SHAP background ($n = 24$ subset)				(d) Seed budget curve			
Background	Estimator	Optimality gap	Spearman	Seeds	Estimator	Optimality gap	Spearman
uniform	SF	0.0015	0.9496	2	CM	0.0000	0.9368
empirical	SF	0.0015	0.9420	2	SF	0.0000	0.9368
CM ref	CM	0.0020	0.8074	4	CM	0.0023	0.9021
				4	SF	0.0023	0.9021
				8	CM	0.0007	0.9508
				8	SF	0.0007	0.9508
				16	CM	0.0017	0.9602
				16	SF	0.0017	0.9602

repeatedly emerged as advantageous. Weight decay L_2 displayed negligible or flat effects. Increasing epochs produced gradual but stable improvements. While effect magnitudes and confidence interval overlaps varied across datasets, the relative ranking of factor importance remained broadly consistent.

Interaction plots visualize deviations caused by factor-pair combinations. In this study, interaction strength was summarized using the PCI metric and displayed as heatmaps. The most prominent interaction appeared between learning rate and batch size, followed by optimizer and learning rate. Interactions involving L_2 were generally weak. These patterns reinforce the main-effect interpretation, suggesting that learning rate and batch size serve as primary decision axes, with other factors acting as secondary adjustments.

As representative examples, Figures 1 and 2 present the main and interaction effect plots for the UCI Concrete dataset. Full sets of figures and metrics for all datasets are provided in Appendix B.

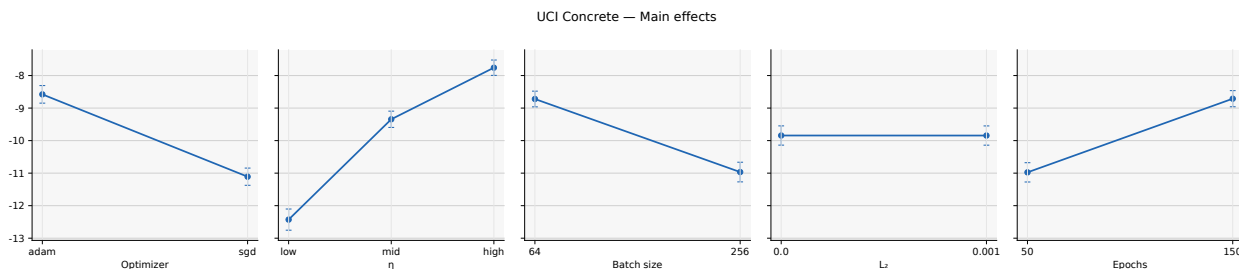


Figure 1: Main-effect plots for the UCI Concrete dataset. Adam and higher learning-rate levels dominate, while smaller batch sizes repeatedly show advantages. The influence of L_2 remains negligible or flat.

8.2 Performance Maps and Interpretability from Two-Factor Approximation

Compressing a complex hyperparameter space into a map that retains only main effects and pairwise interactions makes it possible to immediately see why and where the response function changes. Main-effect plots reveal the average direction and magnitude of influence for each factor through slope patterns and gaps across levels. Interaction plots highlight deviations that cannot be explained additively when two factors vary together, visible through non-parallel lines, diverging gaps, or crossing points. Taken together, these two visualizations complement each other, leaving little blind spot in interpretation.

The strengths of main-effect plots are clear. First, they reveal monotonic increases, monotonic decreases, plateaus, or reversals, providing a rationale for choosing baseline settings. Second, the absolute slope indicates priority, guiding where to densify the grid. Third, confidence intervals quantify both expected gains from level changes and the risks of decision-making. Fourth, by standardizing metrics within each dataset, factors across tasks can be compared on a

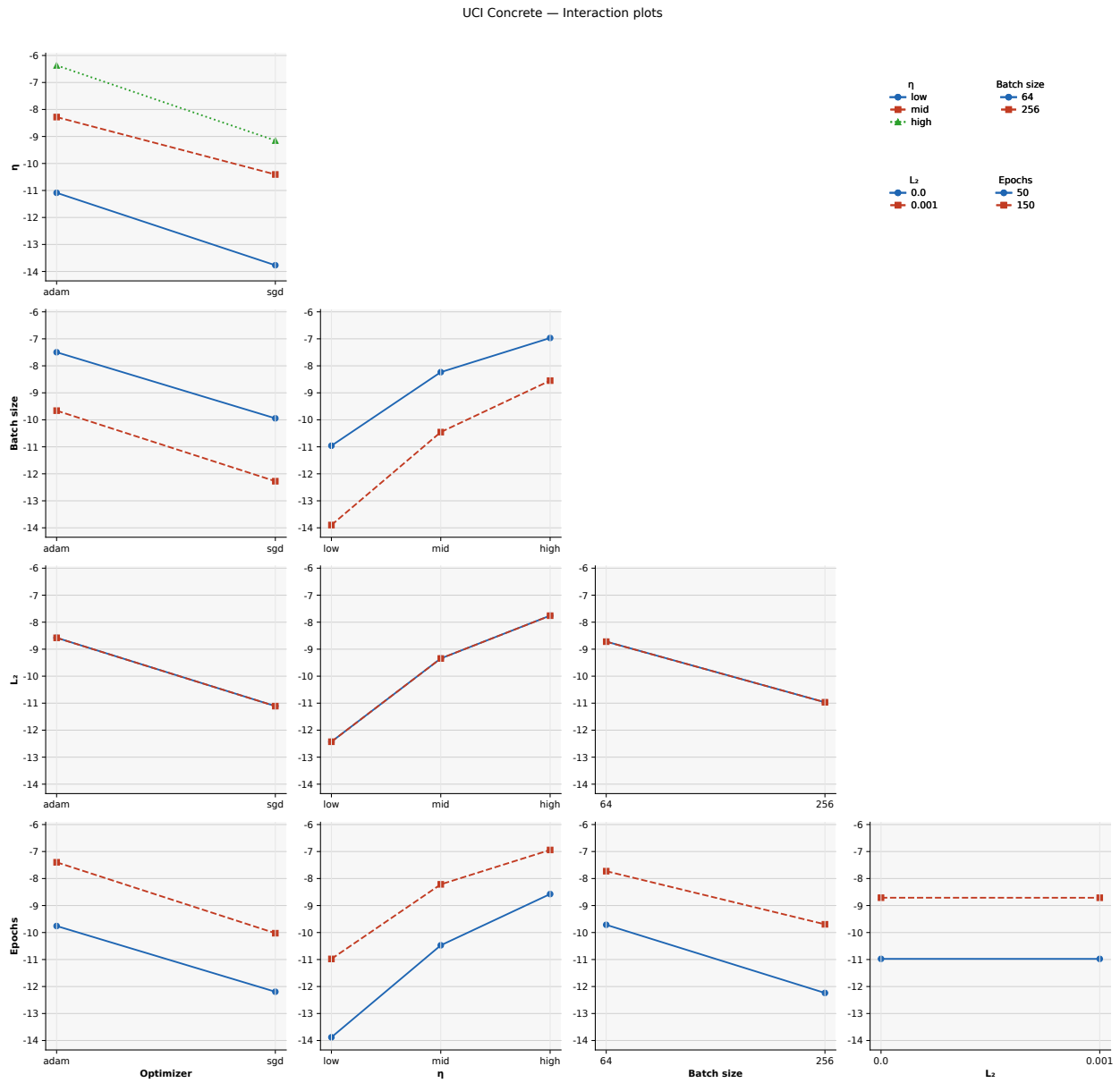


Figure 2: PCI-based interaction plots for the UCI Concrete dataset. The strongest interaction arises from learning rate and batch size, followed by optimizer and learning rate. Interactions involving L_2 are generally weak.

common scale. A single figure thus conveys directional and uncertainty information that cannot be captured by tables or raw numbers alone.

Interaction plots reduce wasted exploration. Nearly parallel lines indicate that two factors can be tuned independently. Large vertical gaps suggest that local grids should be concentrated on those pairs. Line crossings signal that outcomes may depend on setting order, while slope differences point to which factor dominates sensitivity. PCI values, encoded by color or line thickness, provide a quantitative index of which pairs drive performance variation. Selecting such priority pairs significantly reduces sample complexity compared to exhaustive search.

The combined procedure is straightforward. Begin with the steepest slopes in the main-effect plots to set a baseline configuration. Next, refine locally around two or three pairs with the strongest interactions. Flat-effect factors can be fixed, shrinking the search space. Inflection points and widening confidence intervals in the epoch curves help detect diminishing returns. Because the method is repeatable across datasets and models, results remain reusable and auditable.

Diagnostic capability is also strong. Wide error bars highlight regions with high seed-to-seed variability. Oscillations near boundaries indicate potential discretization artifacts. Flat curves, as with L_2 , identify axes that can be deprioritized in tuning and reported concisely. Conversely, strongly diverging pairs such as learning rate and batch size explain exceptions to baseline recipes and should be recorded as such. These records directly support reproducibility documentation and future configuration changes.

Limitations remain: higher-order interactions involving three or more factors may persist as residuals. However, theoretical error bounds and sample complexity analysis constrain their magnitude, and safety can be maintained by selectively expanding checks to a few top pairs. In summary, main and interaction plots condense thousands of configurations into a handful of curves and line bundles, simultaneously conveying directionality, joint effects, and decision risks. They provide high interpretability and consistent search strategies at low cost.

8.3 Consistency, Robustness, and Background Selection of CM and SF Paths

The CM path estimates main and interaction effects directly from conditional means. For each factor, it computes level-specific averages, then applies centering and constraints so that their sum is zero. The SF path, in contrast, collects SHAP contributions at the sample level and fits them via least squares to a model consisting of main and two-factor terms, thereby recovering the same functional surface. The key is that both paths project onto the same model space.

When the background distribution and centering rules are aligned, the two paths converge to the same two-factor surface. With sufficient samples, CM's cell averages and SF's least-squares solutions point to identical main-effect vectors and interaction matrices. This conclusion is supported by the approximation and error decomposition results in the theory section. Convergence is checked by monitoring cosine similarity and rank agreement of effect vectors, along with the size of projection residuals.

From a robustness perspective, CM is sensitive to imbalance in the design. Low-frequency levels yield high variance, and empty cells require imputation. Weighted least squares, shrinkage estimation, and shared contrast constraints help stabilize estimates. SF faces different risks: sampling noise from the background distribution and variance from the number of permutations. Increasing repetitions ensures convergence but raises computational cost. Reusing moments, fixing random seeds, and applying median-of-means techniques improve stability. In the presence of outliers, CM averages can shift, whereas SF tends to be more stable thanks to the contribution-preservation property. Conversely, with extreme imbalance, SF's background samples may overweight majority levels and miss signals from sparse ones. The two paths are complementary, and stability is achieved by tuning weights, truncation, and repetition counts.

Choosing a background distribution should match the interpretive goal. A uniform DoE distribution ensures equal weighting of all levels, supporting fair design comparisons and policy mapping. An operational distribution reflects actual deployment conditions, providing directly actionable estimates. A stress distribution highlights sensitivity in risky regions, useful for conservative boundaries. Since both SHAP contributions and conditional means shift with the distribution, the surface itself changes. As a reporting principle, both uniform DoE and operational backgrounds should be presented, with summary indicators of their differences. If discrepancies are large, additional sensitivity analyses focused on top interaction pairs should be conducted.

Reporting and diagnostics begin by comparing effect estimates under the same constraints. Checks include whether main-effect signs and ranks match, whether the top interaction pairs overlap, and whether projection residuals are small enough to justify the two-factor approximation. Metadata such as background distribution, sample size, seeds, weighting rules, and truncation rules must be documented. Any discrepancies between maps should be decomposed into causes: imbalance, background mismatch, or higher-order residuals.

In summary, CM is simple and computationally light, while SF preserves contributions and is more resilient to model mismatch. Under the same background and constraints, both converge to the same two-factor surface. The safest practice is to specify the background explicitly and use both paths jointly for cross-validation. CM serves as the default for broad exploration, while SF is selectively reinforced in regions with large residuals or high PCI, balancing cost and performance.

8.4 Limitations and Extensions: Higher-Order Interactions, Continuous Factors, and Sequential Design

The two-factor approximation offers an efficient way to read broad search spaces, but it inherently omits synergies or conflicts that arise when three or more axes operate simultaneously. The error decomposition in §5.3 and the optimality gap bounds in §5.4 specify conditions under which this residual remains small. However, when data are sparse or nonlinearity in factor combinations is strong, the safe range may be exceeded. To detect such cases, one should jointly inspect projection residuals on the two-factor surface and the tail of the PCI distribution. When large residuals appear, a local three-factor check can be performed around the implicated pairs. Selection should proceed conservatively: apply hierarchical constraints under sparsity assumptions, and extend to higher-order models only when necessary.

Discretizing continuous factors into finite levels can introduce distortions from boundary choices. Near boundaries, curves may oscillate or samples may cluster unevenly, exaggerating or flattening slopes of main and interaction effects. To mitigate this, balanced quantile splits are used by default, with additional smoothing between adjacent levels. Connecting bin centers via splines or trend filtering aligns CM’s cell means and SF’s contribution sums into consistent shapes. For axes expected to follow monotone trends, monotonic constraints with equality allowance help suppress spurious fluctuations. By explicitly reporting normalization standards, metric orientations, and sensitivity to boundary re-partitioning, interpretive boundaries become clearer. Further extensions include spline-based GAMs or Gaussian processes, which directly estimate smooth effect functions.

Sequential design improves budget efficiency compared to fixed grids. Initially, samples are spread widely; subsequent points are selected using lower bounds of the objective and maps of uncertainty. Main-effect slopes guide the choice of base configurations, while pairs with high PCI receive denser local coverage. Seeds are concentrated on top candidates to quickly shrink local standard errors. Exploration halts once the confidence intervals of the top two candidates are separated. Whether to add new design points or increase seeds is decided by comparing marginal improvement per unit cost, enabling convergence near the optimum without exhaustive search.

Background distribution choice governs both limitations and extensions. A uniform DoE distribution ensures fairness in design comparisons, but misalignment with operational environments raises extrapolation risk. Presenting both uniform and operational distributions side by side reveals sensitivity to distribution shifts. Large discrepancies often indicate hidden higher-order interactions or boundary-sensitive regions. These regions should be prioritized for local extensions and distributional sensitivity analyses.

Independence assumptions also warrant scrutiny. For theoretical convenience, factor independence was assumed, but in practice, strongly coupled factors—such as optimizer and learning-rate schedule—may exist. In such cases, orthogonality and interpretability of the decomposition can change. Diagnosing correlation structures and considering decompositions that permit dependencies are therefore essential. This issue connects to PCI interpretation in §5.5, where interpretive caveats are emphasized.

From a computational perspective, trade-offs between paths must be made explicit. CM is lightweight and well-suited for broad scanning, while SF is more resilient to background bias but slower due to Monte Carlo sampling. A pragmatic compromise is to use CM for wide exploration, then selectively reinforce SF in regions with large residuals or high PCI, balancing cost against performance.

As a result, increasing model complexity rapidly inflates variance and sample complexity. Safety lies in first fixing the portion explained at lower order, then raising the order only in regions where residuals concentrate. Reporting should include effect estimates under consistent constraints, projection residuals, distribution choices, and budget usage. This ensures that the speed and interpretability of the two-factor approximation are preserved, while controlling distortions from higher-order interactions, continuous factors, and sequential design.

9 Conclusion

We proposed FACTORS, a framework that combines design of experiments with Shapley-based decomposition to stably estimate main and two-factor interaction effects of training variables, and to connect these estimates to a risk- and cost-adjusted objective function that directly yields actionable optimal configurations. To ensure fair comparison across heterogeneous factor spaces and designs, we standardized estimates, applied bias correction, and quantified

uncertainty to guide budget requirements. A lightweight search procedure enabled timely decisions even in large factor spaces. Effect estimation was implemented through two complementary paths: conditional means and least-squares reconstruction from sampled Shapley contributions. Including two-factor interactions was shown to markedly improve rank preservation and optimal configuration identification while reducing decision risk. Moreover, summarizing main and interaction effects as maps highlights adjustment priorities and suggests safe improvement paths under cost constraints. Limitations remain: higher-order interactions can persist as residuals, calling for local validation and stepwise extension, and discretization of continuous factors may introduce distortions that can be mitigated by smoothing or monotonic constraints. Overall, FACTORS provides a tuning foundation that jointly offers interpretable evidence and robust performance gains under limited budgets, with natural extensions toward selective higher-order modeling and budget-adaptive sequential design.

Reproducibility Statement

Repository. All code, configs, and scripts are available at github.com/AndrewKim1997/FACTORS (MIT license). We provide a stable tag for the camera-ready version and run CI on every commit.

Data. All datasets are public: UCI *Concrete* (regression), UCI *Car Evaluation* (classification), and *Fashion-MNIST* (via `torchvision`). A one-shot downloader (`scripts/download_data.sh`) and a data policy (`data/README.md`) are included; large files are not tracked by Git.

Environments. Experiments run on Python 3.10–3.12. We ship Conda (`envs/conda-{cpu,gpu}.yaml`) and pip files (`envs/pip-{cpu,gpu}.txt`). For bit-for-bit environments, we provide Dockerfiles for CPU and GPU and build/push images via a dedicated Docker CI workflow.

Determinism & randomness. We fix seeds in all experiments (default seed set: `{0,1,2,3,4}`) and expose a `-seed` flag. Where applicable, deterministic backends (e.g., PyTorch) are enabled via utilities in `src/factors/utils.py`. Bootstrap intervals introduce expected sampling variability; hence we report CIs and aggregate across seeds. Minor numerical differences across platforms (BLAS, GPU kernels) may occur but do not affect qualitative conclusions.

How to reproduce.

1. *Clone the repository:* `git clone https://github.com/AndrewKim1997/FACTORS && cd FACTORS`
2. *Install an environment* (Conda or Docker).
3. *Fetch public datasets:* `bash scripts/download_data.sh concrete car fmnist`
4. *Reproduce main tables/figures:* `bash scripts/reproduce_all.sh` (iterates `configs/runs/main.yaml`).
5. *Run a single experiment:*
`python scripts/run_experiment.py -config configs/datasets/concrete.yaml`
`-seed 0 -out experiments/sanity/concrete/seed_0`

Each run writes self-contained artifacts under `experiments/...` (metrics, score matrices, bootstrap CIs, metadata). Post-processing is handled by `scripts/make_tables_figs.py`, which aggregates results into `results/`.

What is included. (i) Source for the CM (cell-mean) and SF (SHAP-fit) paths, scoring, PCI, optimizers, and uncertainty; (ii) dataset/ablation/run YAMLs used in the paper; (iii) drivers and utilities; (iv) unit tests (`tests/unit`) and a CI-aligned end-to-end sanity test (`tests/integration`).

Compute & expected runtime. Tabular experiments (Concrete, Car) run on CPU within minutes per seed on a modern laptop/VM. Fashion-MNIST benefits from a single CUDA-capable GPU but also includes a reduced CPU “sanity” configuration for CI. We record hardware and timing for every run in `run_metadata.json` (commit, Python/version, device).

Artifact integrity. We log provenance for every figure/table (input metric glob, generation timestamp, commit) and optionally verify dataset checksums (`data/ hashes.json`). Docker image digests are recorded by the Docker CI.

Ethics & third-party assets. All datasets are public and used under their original licenses; no personally identifiable information is introduced by our processing.

Limitations. Exact numerical replication across different hardware/OS may vary slightly due to linear algebra backends and GPU kernels. We mitigate this with fixed seeds, deterministic flags, multiple seeds, and reporting of confidence intervals.

References

- [1] National Institute of Standards and Technology. Artificial intelligence risk management framework (ai rmf 1.0), 2023.
- [2] Organisation for Economic Co-operation and Development. Recommendation of the council on artificial intelligence, 2019.
- [3] European Union. Regulation (eu) 2024/1689 of the european parliament and of the council of 13 june 2024 laying down harmonised rules on artificial intelligence (artificial intelligence act). Official Journal of the European Union, July 2024. OJ L, 12 July 2024.
- [4] International Organization for Standardization (ISO) and International Electrotechnical Commission (IEC). Information technology — artificial intelligence — risk management, 2023.
- [5] International Organization for Standardization (ISO) and International Electrotechnical Commission (IEC). Software engineering — systems and software quality requirements and evaluation (square) — quality model for ai systems, 2023.
- [6] David Sculley, Gary Holt, Daniel Golovin, Eugene Davydov, Todd Phillips, Dietmar Ebner, Vinay Chaudhary, Michael Young, Jean-Francois Crespo, and Dan Dennison. Hidden technical debt in machine learning systems. *Advances in neural information processing systems*, 28, 2015.
- [7] Eric Breck, Shanqing Cai, Eric Nielsen, Michael Salib, and D Sculley. The ml test score: A rubric for ml production readiness and technical debt reduction. In *2017 IEEE international conference on big data (big data)*, pages 1123–1132. IEEE, 2017.
- [8] Denis Baylor, Eric Breck, Heng-Tze Cheng, Noah Fiedel, Chuan Yu Foo, Zakaria Haque, Salem Haykal, Mustafa Ispir, Vihan Jain, Levent Koc, et al. Tfx: A tensorflow-based production-scale machine learning platform. In *Proceedings of the 23rd ACM SIGKDD international conference on knowledge discovery and data mining*, pages 1387–1395, 2017.
- [9] Peter Mattson, Christine Cheng, Gregory Damos, Cody Coleman, Paulius Micikevicius, David Patterson, Hanlin Tang, Gu-Yeon Wei, Peter Bailis, Victor Bittorf, et al. Mlperf training benchmark. *Proceedings of Machine Learning and Systems*, 2:336–349, 2020.
- [10] Benjamin Recht, Rebecca Roelofs, Ludwig Schmidt, and Vaishaal Shankar. Do imagenet classifiers generalize to imagenet? In *International conference on machine learning*, pages 5389–5400. PMLR, 2019.
- [11] Peter Henderson, Riashat Islam, Philip Bachman, Joelle Pineau, Doina Precup, and David Meger. Deep reinforcement learning that matters. In *Proceedings of the AAAI conference on artificial intelligence*, volume 32, 2018.
- [12] Liam Li and Ameet Talwalkar. Random search and reproducibility for neural architecture search. In *Uncertainty in artificial intelligence*, pages 367–377. PMLR, 2020.
- [13] Jared Kaplan, Sam McCandlish, Tom Henighan, Tom B Brown, Benjamin Chess, Rewon Child, Scott Gray, Alec Radford, Jeffrey Wu, and Dario Amodei. Scaling laws for neural language models. *arXiv preprint arXiv:2001.08361*, 2020.
- [14] Jordan Hoffmann, Sebastian Borgeaud, Arthur Mensch, Elena Buchatskaya, Trevor Cai, Eliza Rutherford, Diego de Las Casas, Lisa Anne Hendricks, Johannes Welbl, Aidan Clark, et al. Training compute-optimal large language models. In *Proceedings of the 36th International Conference on Neural Information Processing Systems*, pages 30016–30030, 2022.
- [15] McKinsey & Company. The state of ai: How organizations are rewiring to capture value, 2025.
- [16] PricewaterhouseCoopers. 2025 global digital trust insights: Bridging the gaps to cyber resilience, 2024.
- [17] Boston Consulting Group. Data dominates: How data can create competitive advantage, 2020.
- [18] Jerome Sacks, William J Welch, Toby J Mitchell, and Henry P Wynn. Design and analysis of computer experiments. *Statistical science*, 4(4):409–423, 1989.
- [19] Michael D McKay, Richard J Beckman, and William J Conover. A comparison of three methods for selecting values of input variables in the analysis of output from a computer code. *Technometrics*, 42(1):55–61, 2000.

- [20] Michael Stein. Large sample properties of simulations using latin hypercube sampling. *Technometrics*, 29(2):143–151, 1987.
- [21] Robin L Plackett and J Peter Burman. The design of optimum multifactorial experiments. *Biometrika*, 33(4):305–325, 1946.
- [22] Max D Morris. Factorial sampling plans for preliminary computational experiments. *Technometrics*, 33(2):161–174, 1991.
- [23] Boxin Tang. Orthogonal array-based latin hypercubes. *Journal of the American statistical association*, 88(424):1392–1397, 1993.
- [24] Max D Morris and Toby J Mitchell. Exploratory designs for computational experiments. *Journal of statistical planning and inference*, 43(3):381–402, 1995.
- [25] V Roshan Joseph, Evren Gul, and Shan Ba. Maximum projection designs for computer experiments. *Biometrika*, 102(2):371–380, 2015.
- [26] Donald R Jones, Matthias Schonlau, and William J Welch. Efficient global optimization of expensive black-box functions. *Journal of Global optimization*, 13(4):455–492, 1998.
- [27] Bobak Shahriari, Kevin Swersky, Ziyu Wang, Ryan P Adams, and Nando De Freitas. Taking the human out of the loop: A review of bayesian optimization. *Proceedings of the IEEE*, 104(1):148–175, 2015.
- [28] Jasper Snoek, Hugo Larochelle, and Ryan P Adams. Practical bayesian optimization of machine learning algorithms. *Advances in neural information processing systems*, 25, 2012.
- [29] James Bergstra and Yoshua Bengio. Random search for hyper-parameter optimization. *The journal of machine learning research*, 13(1):281–305, 2012.
- [30] James Bergstra, Rémi Bardenet, Yoshua Bengio, and Balázs Kégl. Algorithms for hyper-parameter optimization. *Advances in neural information processing systems*, 24, 2011.
- [31] Lisha Li, Kevin Jamieson, Giulia DeSalvo, Afshin Rostamizadeh, and Ameet Talwalkar. Hyperband: A novel bandit-based approach to hyperparameter optimization. *Journal of Machine Learning Research*, 18(185):1–52, 2018.
- [32] Stefan Falkner, Aaron Klein, and Frank Hutter. Bobb: Robust and efficient hyperparameter optimization at scale. In *International conference on machine learning*, pages 1437–1446. PMLR, 2018.
- [33] Aaron Klein, Stefan Falkner, Simon Bartels, Philipp Hennig, and Frank Hutter. Fast bayesian optimization of machine learning hyperparameters on large datasets. In *Artificial intelligence and statistics*, pages 528–536. PMLR, 2017.
- [34] Kirthevasan Kandasamy, Gautam Dasarathy, Junier B Oliva, Jeff Schneider, and Barnabás Póczos. Gaussian process bandit optimisation with multi-fidelity evaluations. *Advances in neural information processing systems*, 29, 2016.
- [35] Daniel Golovin, Benjamin Solnik, Subhodeep Moitra, Greg Kochanski, John Karro, and David Sculley. Google vizier: A service for black-box optimization. In *Proceedings of the 23rd ACM SIGKDD international conference on knowledge discovery and data mining*, pages 1487–1495, 2017.
- [36] Marco Tulio Ribeiro, Sameer Singh, and Carlos Guestrin. " why should i trust you?" explaining the predictions of any classifier. In *Proceedings of the 22nd ACM SIGKDD international conference on knowledge discovery and data mining*, pages 1135–1144, 2016.
- [37] Scott M Lundberg and Su-In Lee. A unified approach to interpreting model predictions. *Advances in neural information processing systems*, 30, 2017.
- [38] Mukund Sundararajan, Ankur Taly, and Qiqi Yan. Axiomatic attribution for deep networks. In *International conference on machine learning*, pages 3319–3328. PMLR, 2017.
- [39] Avanti Shrikumar, Peyton Greenside, and Anshul Kundaje. Learning important features through propagating activation differences. In *International conference on machine learning*, pages 3145–3153. PMIR, 2017.
- [40] Sebastian Bach, Alexander Binder, Grégoire Montavon, Frederick Klauschen, Klaus-Robert Müller, and Wojciech Samek. On pixel-wise explanations for non-linear classifier decisions by layer-wise relevance propagation. *PLoS one*, 10(7):e0130140, 2015.
- [41] Ramprasaath R Selvaraju, Michael Cogswell, Abhishek Das, Ramakrishna Vedantam, Devi Parikh, and Dhruv Batra. Grad-cam: Visual explanations from deep networks via gradient-based localization. In *Proceedings of the IEEE international conference on computer vision*, pages 618–626, 2017.

- [42] Daniel Smilkov, Nikhil Thorat, Been Kim, Fernanda Viégas, and Martin Wattenberg. Smoothgrad: removing noise by adding noise. *arXiv preprint arXiv:1706.03825*, 2017.
- [43] Ruth C Fong and Andrea Vedaldi. Interpretable explanations of black boxes by meaningful perturbation. In *Proceedings of the IEEE international conference on computer vision*, pages 3429–3437, 2017.
- [44] Matthew D Zeiler and Rob Fergus. Visualizing and understanding convolutional networks. In *European conference on computer vision*, pages 818–833. Springer, 2014.
- [45] Scott M Lundberg, Gabriel Erion, Hugh Chen, Alex DeGrave, Jordan M Prutkin, Bala Nair, Ronit Katz, Jonathan Himmelfarb, Nisha Bansal, and Su-In Lee. From local explanations to global understanding with explainable ai for trees. *Nature machine intelligence*, 2(1):56–67, 2020.
- [46] Mukund Sundararajan and Amir Najmi. The many shapley values for model explanation. In *International conference on machine learning*, pages 9269–9278. PMLR, 2020.
- [47] Mukund Sundararajan, Kedar Dhamdhere, and Ashish Agarwal. The shapley taylor interaction index. In *International conference on machine learning*, pages 9259–9268. PMLR, 2020.
- [48] Marco Tulio Ribeiro, Sameer Singh, and Carlos Guestrin. Anchors: High-precision model-agnostic explanations. In *Proceedings of the AAAI conference on artificial intelligence*, volume 32, 2018.
- [49] Leo Breiman. Random forests. *Machine learning*, 45(1):5–32, 2001.
- [50] André Altmann, Laura Toloşi, Oliver Sander, and Thomas Lengauer. Permutation importance: a corrected feature importance measure. *Bioinformatics*, 26(10):1340–1347, 2010.
- [51] Kjersti Aas, Martin Jullum, and Anders Løland. Explaining individual predictions when features are dependent: More accurate approximations to shapley values. *Artificial Intelligence*, 298:103502, 2021.
- [52] Ian Covert, Scott Lundberg, and Su-In Lee. Explaining by removing: A unified framework for model explanation. *Journal of Machine Learning Research*, 22(209):1–90, 2021.
- [53] Julius Adebayo, Justin Gilmer, Michael Muelly, Ian Goodfellow, Moritz Hardt, and Been Kim. Sanity checks for saliency maps. *Advances in neural information processing systems*, 31, 2018.
- [54] Sara Hooker, Dumitru Erhan, Pieter-Jan Kindermans, and Been Kim. A benchmark for interpretability methods in deep neural networks. *Advances in neural information processing systems*, 32, 2019.
- [55] Cynthia Rudin. Stop explaining black box machine learning models for high stakes decisions and use interpretable models instead. *Nature machine intelligence*, 1(5):206–215, 2019.
- [56] Amirata Ghorbani, Abubakar Abid, and James Zou. Interpretation of neural networks is fragile. In *Proceedings of the AAAI conference on artificial intelligence*, volume 33, pages 3681–3688, 2019.
- [57] Ann-Kathrin Dombrowski, Maximilian Alber, Christopher Anders, Marcel Ackermann, Klaus-Robert Müller, and Pan Kessel. Explanations can be manipulated and geometry is to blame. *Advances in neural information processing systems*, 32, 2019.
- [58] Dylan Slack, Sophie Hilgard, Emily Jia, Sameer Singh, and Himabindu Lakkaraju. Fooling lime and shap: Adversarial attacks on post hoc explanation methods. In *Proceedings of the AAAI/ACM Conference on AI, Ethics, and Society*, pages 180–186, 2020.
- [59] Alon Jacovi and Yoav Goldberg. Towards faithfully interpretable nlp systems: How should we define and evaluate faithfulness? In *Proceedings of the 58th Annual Meeting of the Association for Computational Linguistics*, pages 4198–4205, 2020.
- [60] Peter Hase and Mohit Bansal. Evaluating explainable ai: Which algorithmic explanations help users predict model behavior? In *Proceedings of the 58th Annual Meeting of the Association for Computational Linguistics*, pages 5540–5552, 2020.
- [61] Sarthak Jain and Byron C Wallace. Attention is not explanation. In *Proceedings of the 2019 Conference of the North American Chapter of the Association for Computational Linguistics: Human Language Technologies, Volume 1 (Long and Short Papers)*, pages 3543–3556, 2019.
- [62] Sarah Wiegreffe and Yuval Pinter. Attention is not not explanation. In *Proceedings of the 2019 Conference on Empirical Methods in Natural Language Processing and the 9th International Joint Conference on Natural Language Processing (EMNLP-IJCNLP)*, pages 11–20, 2019.
- [63] Forough Poursabzi-Sangdeh, Daniel G Goldstein, Jake M Hofman, Jennifer Wortman Vaughan, and Hanna Wallach. Manipulating and measuring model interpretability. In *Proceedings of the 2021 CHI conference on human factors in computing systems*, pages 1–52, 2021.

- [64] Gagan Bansal, Tongshuang Wu, Joyce Zhou, Raymond Fok, Besmira Nushi, Ece Kamar, Marco Tulio Ribeiro, and Daniel Weld. Does the whole exceed its parts? the effect of ai explanations on complementary team performance. In *Proceedings of the 2021 CHI conference on human factors in computing systems*, pages 1–16, 2021.
- [65] Xinru Wang and Ming Yin. Are explanations helpful? a comparative study of the effects of explanations in ai-assisted decision-making. In *Proceedings of the 26th International Conference on Intelligent User Interfaces*, pages 318–328, 2021.
- [66] Harmanpreet Kaur, Harsha Nori, Samuel Jenkins, Rich Caruana, Hanna Wallach, and Jennifer Wortman Vaughan. Interpreting interpretability: understanding data scientists’ use of interpretability tools for machine learning. In *Proceedings of the 2020 CHI conference on human factors in computing systems*, pages 1–14, 2020.
- [67] Frank Hutter, Holger Hoos, and Kevin Leyton-Brown. An efficient approach for assessing hyperparameter importance. In *International conference on machine learning*, pages 754–762. PMLR, 2014.
- [68] Marcel Wever, Maximilian Muschalik, Fabian Fumagalli, and Marius Lindauer. Hypershap: Shapley values and interactions for hyperparameter importance. *arXiv preprint arXiv:2502.01276*, 2025.
- [69] Eunhye Song, Barry L Nelson, and Jeremy Staum. Shapley effects for global sensitivity analysis: Theory and computation. *SIAM/ASA Journal on Uncertainty Quantification*, 4(1):1060–1083, 2016.
- [70] Amirata Ghorbani and James Zou. Data shapley: Equitable valuation of data for machine learning. In *International conference on machine learning*, pages 2242–2251. PMLR, 2019.
- [71] Yongchan Kwon and James Zou. Beta shapley: a unified and noise-reduced data valuation framework for machine learning. In *International Conference on Artificial Intelligence and Statistics*, pages 8780–8802. PMLR, 2022.
- [72] Garima Pruthi, Frederick Liu, Satyen Kale, and Mukund Sundararajan. Estimating training data influence by tracing gradient descent. *Advances in Neural Information Processing Systems*, 33:19920–19930, 2020.
- [73] Pang Wei Koh and Percy Liang. Understanding black-box predictions via influence functions. In *International conference on machine learning*, pages 1885–1894. PMLR, 2017.
- [74] Amirata Ghorbani and James Y Zou. Neuron shapley: Discovering the responsible neurons. *Advances in neural information processing systems*, 33:5922–5932, 2020.
- [75] Priya Goyal, Piotr Dollár, Ross Girshick, Pieter Noordhuis, Lukasz Wesolowski, Aapo Kyrola, Andrew Tulloch, Yangqing Jia, and Kaiming He. Accurate, large minibatch sgd: Training imagenet in 1 hour. *arXiv preprint arXiv:1706.02677*, 2017.
- [76] Samuel L Smith, Pieter-Jan Kindermans, Chris Ying, and Quoc V Le. Don’t decay the learning rate, increase the batch size. *arXiv preprint arXiv:1711.00489*, 2017.
- [77] Nitish Shirish Keskar, Dheevatsa Mudigere, Jorge Nocedal, Mikhail Smelyanskiy, and Ping Tak Peter Tang. On large-batch training for deep learning: Generalization gap and sharp minima. *arXiv preprint arXiv:1609.04836*, 2016.
- [78] Xavier Bouthillier, Pierre Delaunay, Mirko Bronzi, Assya Trofimov, Brennan Nichyporuk, Justin Szeto, Nazanin Mohammadi Sepahvand, Edward Raff, Kanika Madan, Vikram Voleti, et al. Accounting for variance in machine learning benchmarks. *Proceedings of Machine Learning and Systems*, 3:747–769, 2021.
- [79] Keller Jordan. On the variance of neural network training with respect to test sets and distributions. *arXiv preprint arXiv:2304.01910*, 2023.
- [80] Maximilian Muschalik, Hubert Baniecki, Fabian Fumagalli, Patrick Kolpaczki, Barbara Hammer, and Eyke Hüllermeier. shapiq: Shapley interactions for machine learning. *Advances in Neural Information Processing Systems*, 37:130324–130357, 2024.
- [81] Che-Ping Tsai, Chih-Kuan Yeh, and Pradeep Ravikumar. Faith-shap: The faithful shapley interaction index. *Journal of Machine Learning Research*, 24(94):1–42, 2023.
- [82] Jerome H Friedman and Bogdan E Popescu. Predictive learning via rule ensembles. *The Annals of Applied Statistics*, 2(3):916–954, 2008.
- [83] Yin Lou, Rich Caruana, Johannes Gehrke, and Giles Hooker. Accurate intelligible models with pairwise interactions. In *Proceedings of the 19th ACM SIGKDD international conference on Knowledge discovery and data mining*, pages 623–631, 2013.
- [84] Hugh A Chipman, Edward I George, and Robert E McCulloch. Bart: Bayesian additive regression trees. *The Annals of Applied Statistics*, pages 266–298, 2010.

- [85] Ilya M Sobol. Global sensitivity indices for nonlinear mathematical models and their monte carlo estimates. *Mathematics and computers in simulation*, 55(1-3):271–280, 2001.
- [86] Andrea Saltelli. Making best use of model evaluations to compute sensitivity indices. *Computer physics communications*, 145(2):280–297, 2002.
- [87] Jeremy E Oakley and Anthony O’Hagan. Probabilistic sensitivity analysis of complex models: a bayesian approach. *Journal of the Royal Statistical Society Series B: Statistical Methodology*, 66(3):751–769, 2004.
- [88] Art B Owen. Better estimation of small sobol’ sensitivity indices. *ACM Transactions on Modeling and Computer Simulation (TOMACS)*, 23(2):1–17, 2013.
- [89] Alexandre Janon, Thierry Klein, Agnes Lagnoux, Maëlle Nodet, and Clémentine Prieur. Asymptotic normality and efficiency of two sobol index estimators. *ESAIM: Probability and Statistics*, 18:342–364, 2014.
- [90] Gaëlle Chastaing, Fabrice Gamboa, and Clémentine Prieur. Generalized hoeffding-sobol decomposition for dependent variables-application to sensitivity analysis. *Electronic Journal of Statistics*, 6:2420–2448, 2012.
- [91] Nicolas Durrande, David Ginsbourger, Olivier Roustant, and Laurent Carraro. Anova kernels and rkhs of zero mean functions for model-based sensitivity analysis. *Journal of Multivariate Analysis*, 115:57–67, 2013.
- [92] Daria Sorokina, Rich Caruana, Mirek Riedewald, and Daniel Fink. Detecting statistical interactions with additive groves of trees. In *Proceedings of the 25th international conference on Machine learning*, pages 1000–1007, 2008.
- [93] Michael Tsang, Dehua Cheng, and Yan Liu. Detecting statistical interactions from neural network weights. In *International Conference on Learning Representations*, 2018.
- [94] Jacob Bien, Jonathan Taylor, and Robert Tibshirani. A lasso for hierarchical interactions. *Annals of statistics*, 41(3):1111, 2013.
- [95] Giles Hooker. Generalized functional anova diagnostics for high-dimensional functions of dependent variables. *Journal of computational and graphical statistics*, 16(3):709–732, 2007.
- [96] Jacob R Gardner, Matt J Kusner, Zhixiang Eddie Xu, Kilian Q Weinberger, and John P Cunningham. Bayesian optimization with inequality constraints. In *ICML*, volume 2014, pages 937–945, 2014.
- [97] Kevin Swersky, Jasper Snoek, and Ryan P Adams. Multi-task bayesian optimization. *Advances in neural information processing systems*, 26, 2013.
- [98] Matthias Feurer, Aaron Klein, Katharina Eggenberger, Jost Springenberg, Manuel Blum, and Frank Hutter. Efficient and robust automated machine learning. *Advances in neural information processing systems*, 28, 2015.
- [99] Barret Zoph and Quoc V Le. Neural architecture search with reinforcement learning. *arXiv preprint arXiv:1611.01578*, 2016.
- [100] Hanxiao Liu, Karen Simonyan, and Yiming Yang. Darts: Differentiable architecture search. *arXiv preprint arXiv:1806.09055*, 2018.
- [101] Esteban Real, Alok Aggarwal, Yanping Huang, and Quoc V Le. Regularized evolution for image classifier architecture search. In *Proceedings of the aaai conference on artificial intelligence*, volume 33, pages 4780–4789, 2019.
- [102] Yanan Sui, Alkis Gotovos, Joel Burdick, and Andreas Krause. Safe exploration for optimization with gaussian processes. In *International conference on machine learning*, pages 997–1005. PMLR, 2015.
- [103] Sandra Wachter, Brent Mittelstadt, and Chris Russell. Counterfactual explanations without opening the black box: Automated decisions and the gdpr. *Harv. JL & Tech.*, 31:841, 2017.
- [104] Berk Ustun, Alexander Spangher, and Yang Liu. Actionable recourse in linear classification. In *Proceedings of the conference on fairness, accountability, and transparency*, pages 10–19, 2019.
- [105] Ramaravind K Mothilal, Amit Sharma, and Chenhao Tan. Explaining machine learning classifiers through diverse counterfactual explanations. In *Proceedings of the 2020 conference on fairness, accountability, and transparency*, pages 607–617, 2020.
- [106] Amir-Hossein Karimi, Gilles Barthe, Bernhard Schölkopf, and Isabel Valera. A survey of algorithmic recourse: definitions, formulations, solutions, and prospects. *arXiv preprint arXiv:2010.04050*, 2020.

A Proofs and Additional Theory

We provide complete proofs for the definitions and theorems introduced in the main text, along with auxiliary lemmas and technical assumptions not included there. We present detailed concentration bounds for the Monte Carlo approximation of SHAP values and its propagation to the effect table, and we extend convergence and optimality guarantees of the coordinate-based optimizer. Properties of the PCI are further elaborated in terms of centering, scale invariance, and comparability. All notation and conditions follow §3 and §5. Proof sketches in the main text are replaced here with full proofs.

A.1 Functional Decomposition and Alignment with SHAP

Under the assumption that the reference distribution P factorizes across factors, we develop the orthogonality and uniqueness of the functional decomposition and prove how this decomposition is linked to Shapley contributions. Notation follows §3.

Definition A.1 (Subspaces and centering). Let $\mathcal{H} = L^2(\mathcal{X}, P)$ with inner product $\langle u, v \rangle = \mathbb{E}_P[uv]$. Define the constant subspace $\mathcal{H}_0 = \{c : c \in \mathbb{R}\}$. For each factor j ,

$$\mathcal{H}_j = \left\{ h(X_j) : \mathbb{E}[h(X_j)] = 0 \right\},$$

and for each pair of distinct factors $j \neq k$,

$$\mathcal{H}_{jk} = \left\{ h(X_j, X_k) : \mathbb{E}[h | X_j] = 0, \mathbb{E}[h | X_k] = 0 \right\}.$$

Lemma A.2 (Orthogonality). *Under the product distribution assumption, \mathcal{H}_0 , \mathcal{H}_j , and \mathcal{H}_{jk} are mutually orthogonal. More generally, for distinct subsets $S \neq T \subseteq [d]$, any $g_S \in \mathcal{H}_S$ and $g_T \in \mathcal{H}_T$ are orthogonal.*

Proof. Orthogonality between constants and other terms follows from $\mathbb{E}[h] = 0$. For single-factor terms,

$$\mathbb{E}[h_j(X_j)h_k(X_k)] = \mathbb{E}[h_j(X_j)]\mathbb{E}[h_k(X_k)] = 0,$$

since the product distribution implies independence and each factor has mean zero. For a single-factor and a two-factor term with overlapping indices,

$$\mathbb{E}[h_j(X_j)h_{jk}(X_j, X_k)] = \mathbb{E}\left[h_j(X_j) \mathbb{E}[h_{jk}(X_j, X_k) | X_j]\right] = 0,$$

since double-centering ensures the conditional mean is zero. If indices are disjoint,

$$\mathbb{E}[h_j(X_j)h_{\ell m}(X_\ell, X_m)] = \mathbb{E}[h_j(X_j)]\mathbb{E}[h_{\ell m}(X_\ell, X_m)] = 0,$$

again by independence and centering. Orthogonality between two-factor terms follows similarly. The general case for $S \neq T$ is proved in the same way. \square

Proposition A.3 (Functional decomposition: existence and uniqueness). *Every $f \in \mathcal{H}$ admits the decomposition*

$$f(x) = \mu + \sum_{j=1}^d g_j(x_j) + \sum_{1 \leq j < k \leq d} g_{jk}(x_j, x_k) + r(x),$$

where $\mu = \mathbb{E}[f] \in \mathcal{H}_0$, $g_j \in \mathcal{H}_j$, $g_{jk} \in \mathcal{H}_{jk}$, and the remainder r is orthogonal to $\mathcal{H}_0 \oplus (\oplus_j \mathcal{H}_j) \oplus (\oplus_{j < k} \mathcal{H}_{jk})$. The decomposition is unique.

Proof. Consider orthogonal projections:

$$\begin{aligned} \mu &= \Pi_{\mathcal{H}_0} f = \mathbb{E}[f], & g_j &= \Pi_{\mathcal{H}_j} (f - \mu) = \mathbb{E}[f | X_j] - \mu, \\ g_{jk} &= \Pi_{\mathcal{H}_{jk}} \left(f - \mu - \sum_{\ell} g_{\ell} \right) = \mathbb{E}[f | X_j, X_k] - g_j - g_k - \mu. \end{aligned}$$

Direct calculation yields

$$\mathbb{E}[g_j] = 0, \quad \mathbb{E}[g_{jk} | X_j] = 0, \quad \mathbb{E}[g_{jk} | X_k] = 0,$$

hence these lie in the defined subspaces. By Lemma A.2, $\mathcal{V} = \mathcal{H}_0 \oplus (\oplus_j \mathcal{H}_j) \oplus (\oplus_{j < k} \mathcal{H}_{jk})$ is a closed orthogonal sum. Thus

$$f = \Pi_{\mathcal{V}} f + (I - \Pi_{\mathcal{V}})f,$$

with the constructed terms corresponding to $\Pi_{\mathcal{V}} f$. Uniqueness follows from orthogonal projections. \square

Lemma A.4 (Equivalent double-centering). *For any h , the following are equivalent: 1) $\mathbb{E}[h | X_j] = 0$, $\mathbb{E}[h | X_k] = 0$. 2) $\sum_m \pi_{k|j}(m | \ell) h(\ell, m) = 0$ for all ℓ , $\sum_\ell \pi_{j|k}(\ell | m) h(\ell, m) = 0$ for all m .*

Proof. By the definition of conditional expectation in discrete form,

$$\mathbb{E}[h | X_j = \ell] = \sum_m \pi_{k|j}(m | \ell) h(\ell, m), \quad \mathbb{E}[h | X_k = m] = \sum_\ell \pi_{j|k}(\ell | m) h(\ell, m).$$

These are exactly the required equalities. \square

Theorem A.5 (Consistency of FANOVA and Shapley). *Under the product distribution assumption, the FANOVA of f is*

$$f(x) = \mu + \sum_{\emptyset \neq S \subseteq [d]} g_S(x_S), \quad \mathbb{E}[g_S | X_T] = 0 \text{ for all } T \subsetneq S.$$

For any evaluation point x and factor j , the Shapley contribution is

$$\phi_j(x) = \sum_{\substack{S \subseteq [d] \\ j \in S}} \frac{1}{|S|} g_S(x_S).$$

Proof. Consider the coalition function $v(T) = \mathbb{E}[f(x_T, X_{-T})]$. By independence and centering,

$$v(T) = \mu + \sum_{\substack{S \subseteq T \\ S \neq \emptyset}} g_S(x_S).$$

If $S \not\subseteq T$, then at least one coordinate integrates to zero. For a permutation π , the marginal contribution of j is

$$\Delta_j(\pi) = v(\text{Pre}_\pi(j) \cup \{j\}) - v(\text{Pre}_\pi(j)) = \sum_{\substack{S \ni j \\ S \setminus \{j\} \subseteq \text{Pre}_\pi(j)}} g_S(x_S).$$

Taking expectation over π ,

$$\phi_j(x) = \sum_{S \ni j} \Pr(S \setminus \{j\} \subseteq \text{Pre}_\pi(j)) g_S(x_S) = \sum_{S \ni j} \frac{1}{|S|} g_S(x_S),$$

since the probability that j appears last among $|S|$ elements is $1/|S|$. \square

Corollary A.6 (Second-order truncation). *If $f = \mu + \sum_j g_j(x_j) + \sum_{j < k} g_{jk}(x_j, x_k)$, then*

$$\phi_j(x) = g_j(x_j) + \frac{1}{2} \sum_{k \neq j} g_{jk}(x_j, x_k).$$

Proof. In Theorem A.5, only terms with $|S| = 1$ and $|S| = 2$ remain. \square

Proposition A.7 (Efficiency and centering). *The identity $\sum_{j=1}^d \phi_j(x) = f(x) - \mu$ holds. If the centering constraints are satisfied, then the Shapley sum computed from the centered effect table also satisfies efficiency.*

Proof. Summing Theorem A.5 over all j ,

$$\sum_{j=1}^d \phi_j(x) = \sum_{S \neq \emptyset} \left(\sum_{j \in S} \frac{1}{|S|} \right) g_S(x_S) = \sum_{S \neq \emptyset} g_S(x_S) = f(x) - \mu.$$

Centering constraints are $\sum_\ell \pi_j(\ell) g_j(\ell) = 0$ and $\mathbb{E}[g_{jk} | X_j] = \mathbb{E}[g_{jk} | X_k] = 0$, already verified in Lemma A.4 and projection construction. \square

Remark A.8 (Decomposition and orthogonality under dependent backgrounds). If the product independence assumption is relaxed, full orthogonality of the ANOVA decomposition no longer holds. Nonetheless, when a background distribution Q has sufficient support and finite second moments, the second-order projection in the Q -weighted least-squares sense still exists uniquely, and the basis for main and interaction effects remains valid. Theorem A.5 generalizes by replacing the independent product distribution with Q , centering all effects with respect to Q , and applying the same constraints; the resulting formula retains the same form, with coefficients adjusted by the cross-moments of Q .

A.2 Error Decomposition and Sample Complexity

We separate estimation error and truncation error in the two-factor approximation, and present concentration bounds, uniform convergence, and effective sample size bounds for weighted estimation. Notation follows §3 and §5.

Definition A.9 (Error decomposition and notation). Let the estimated effects be $\tilde{g}_j, \tilde{g}_{jk}$ and the true effects be g_j, g_{jk} . With the higher-order remainder denoted by $r(x)$,

$$f(x) = \mu + \sum_j g_j(x_j) + \sum_{j < k} g_{jk}(x_j, x_k) + r(x).$$

Define the estimation error

$$\varepsilon(x) := \sum_j (\tilde{g}_j(x_j) - g_j(x_j)) + \sum_{j < k} (\tilde{g}_{jk}(x_j, x_k) - g_{jk}(x_j, x_k)).$$

Theorem A.10 (Error decomposition of expected performance). *For all x ,*

$$\tilde{f}(x) - f(x) = \varepsilon(x) - r(x), \quad \mathbb{E}_P[(\tilde{f} - f)^2] \leq 2 \mathbb{E}_P[\varepsilon^2] + 2 \mathbb{E}_P[r^2].$$

Proof. From the definitions,

$$\tilde{f}(x) = \hat{\mu} + \sum_j \tilde{g}_j(x_j) + \sum_{j < k} \tilde{g}_{jk}(x_j, x_k), \quad f(x) = \mu + \sum_j g_j(x_j) + \sum_{j < k} g_{jk}(x_j, x_k) + r(x).$$

Subtracting gives

$$\tilde{f} - f = (\hat{\mu} - \mu) + \sum_j (\tilde{g}_j - g_j) + \sum_{j < k} (\tilde{g}_{jk} - g_{jk}) - r.$$

With centering and normalization, we may set $\hat{\mu} = \mu$ without bias, so $\tilde{f} - f = \varepsilon - r$. The second inequality follows by applying $(a - b)^2 \leq 2a^2 + 2b^2$ with $a = \varepsilon, b = r$. \square

Cell means and sample complexity

Lemma A.11 (Boundedness of cell means). *If predictions are bounded by $|f(x)| \leq B$, then the conditional mean for any level pair (ℓ, m) lies in $[-B, B]$.*

Proof. A conditional mean is a linear combination of bounded values, hence inherits the same bounds. \square

Theorem A.12 (Hoeffding bound). *If the cell size for level pair (ℓ, m) is $n_{jk}(\ell, m)$, then for any $\delta \in (0, 1)$,*

$$\Pr\left(\left|\widehat{\mathbb{E}}[f \mid X_j = \ell, X_k = m] - \mathbb{E}[f \mid X_j = \ell, X_k = m]\right| \leq B \sqrt{\frac{2 \log(2/\delta)}{n_{jk}(\ell, m)}}\right) \geq 1 - \delta.$$

Proof. Let $Y_s = f(X^{(s)})$ denote samples within the cell, with $\mathbb{E}[Y_s] = \mathbb{E}[f \mid X_j = \ell, X_k = m]$ and $|Y_s| \leq B$. For $\bar{Y} = \frac{1}{n} \sum Y_s$, Hoeffding's inequality yields $\Pr(|\bar{Y} - \mathbb{E}\bar{Y}| \geq t) \leq 2 \exp(-2nt^2/(2B)^2)$. Substituting $t = B \sqrt{2 \log(2/\delta)/n}$ gives the claim. \square

Theorem A.13 (Bernstein bound). *With cell variance $\sigma_{jk}^2(\ell, m) = \text{Var}(f(X) \mid X_j = \ell, X_k = m)$, with probability $1 - \delta$,*

$$\left|\widehat{\mathbb{E}}[f \mid X_j = \ell, X_k = m] - \mathbb{E}[f \mid X_j = \ell, X_k = m]\right| \leq \sqrt{\frac{2\sigma_{jk}^2(\ell, m) \log(3/\delta)}{n_{jk}(\ell, m)}} + \frac{3B \log(3/\delta)}{n_{jk}(\ell, m)}.$$

Proof. Apply the Bernstein inequality for independent bounded samples: $\Pr(|\bar{Y} - \mathbb{E}\bar{Y}| \geq t) \leq 2 \exp(-nt^2/(2\sigma^2 + 2Bt/3))$. \square

Corollary A.14 (Uniform bound across all cells). *If factors j, k have L_j, L_k levels,*

$$n_{\min} \geq \frac{2B^2}{\epsilon^2} \log\left(\frac{2L_j L_k}{\delta}\right)$$

ensures with probability $1 - \delta$ that the mean error for every cell is at most ϵ .

Proof. Apply Theorem A.12 to each cell and use a union bound. \square

Weighted estimation and effective sample size

Definition A.15 (Weighted mean and effective sample size). For cell (ℓ, m) , normalized weights are $\alpha_i = w_i / \sum w_i$, and the weighted mean is $\sum \alpha_i f^{(i)}$. Define the effective sample size

$$n_{\text{eff}}(\ell, m) = \frac{1}{\sum \alpha_i^2}.$$

Proposition A.16 (Weighted Hoeffding bound). *With probability $1 - \delta$,*

$$\left| \widehat{\mathbb{E}}_w[f \mid X_j = \ell, X_k = m] - \mathbb{E}_w[f \mid X_j = \ell, X_k = m] \right| \leq B \sqrt{2 \log(2/\delta) \sum \alpha_i^2} = B \sqrt{\frac{2 \log(2/\delta)}{n_{\text{eff}}(\ell, m)}}.$$

Proof. For weighted sum $S = \sum \alpha_i Z_i$ with $Z_i \in [-B, B]$ and $\sum \alpha_i = 1$, the weighted Hoeffding inequality states $\Pr(|S - \mathbb{E}S| \geq t) \leq 2 \exp(-2t^2/(4B^2 \sum \alpha_i^2))$. Substituting $t = B \sqrt{2 \log(2/\delta) \sum \alpha_i^2}$ yields the result. \square

Propagation to effect estimates

Lemma A.17 (Error propagation to main and interaction effects). *For each j, ℓ ,*

$$|\hat{g}_j(\ell) - g_j(\ell)| \leq \left| \widehat{\mathbb{E}}[f \mid X_j = \ell] - \mathbb{E}[f \mid X_j = \ell] \right| + |\hat{\mu} - \mu|.$$

For each (j, k, ℓ, m) ,

$$\begin{aligned} |\hat{g}_{jk}(\ell, m) - g_{jk}(\ell, m)| &\leq \left| \widehat{\mathbb{E}}[f \mid X_j = \ell, X_k = m] - \mathbb{E}[f \mid X_j = \ell, X_k = m] \right| \\ &+ \left| \widehat{\mathbb{E}}[f \mid X_j = \ell] - \mathbb{E}[f \mid X_j = \ell] \right| + \left| \widehat{\mathbb{E}}[f \mid X_k = m] - \mathbb{E}[f \mid X_k = m] \right| + |\hat{\mu} - \mu|. \end{aligned}$$

Proof. Subtract definitions of g_j and g_{jk} and apply the triangle inequality. \square

Theorem A.18 (Uniform error of the effect table). *If all single-level and pairwise mean errors are within ϵ_1 and $|\hat{\mu} - \mu| \leq \epsilon_0$, then*

$$\sup_{\ell} |\hat{g}_j(\ell) - g_j(\ell)| \leq \epsilon_1 + \epsilon_0, \quad \sup_{\ell, m} |\hat{g}_{jk}(\ell, m) - g_{jk}(\ell, m)| \leq 3\epsilon_1 + \epsilon_0.$$

Proof. Bounding the right-hand side of Lemma A.17 by maxima yields the claim. \square

Deviation of approximation and objective

Theorem A.19 (Uniform deviation of \tilde{f}). *For all x ,*

$$\left| \tilde{f}(x) - \mu - \sum_j g_j(x_j) - \sum_{j < k} g_{jk}(x_j, x_k) \right| \leq \sum_j \sup_{\ell} |\tilde{g}_j(\ell) - g_j(\ell)| + \sum_{j < k} \sup_{\ell, m} |\tilde{g}_{jk}(\ell, m) - g_{jk}(\ell, m)|.$$

With shrinkage $\tilde{g} = \eta \hat{g}$, $\tilde{g} - g = \eta(\hat{g} - g) + (1 - \eta)g$, so the error splits as $|\eta| \|\hat{g} - g\|_{\infty} + |1 - \eta| \|g\|_{\infty}$.

Proof. Apply the triangle inequality term by term, and expand the shrinkage decomposition. \square

Corollary A.20 (Uniform deviation of the objective). *If the risk and cost terms are independent of estimation,*

$$\sup_{x \in \Omega} |\hat{J}(x) - J(x)| \leq \sum_j \sup_{\ell} |\tilde{g}_j(\ell) - g_j(\ell)| + \sum_{j < k} \sup_{\ell, m} |\tilde{g}_{jk}(\ell, m) - g_{jk}(\ell, m)|.$$

Proof. Use the definition $J = \tilde{f} - \text{risk} - \text{cost}$ and substitute Theorem A.19. \square

Risk decomposition under shrinkage

Proposition A.21 (Mean squared risk of Laplace-type shrinkage). *If $\tilde{g} = \eta\hat{g}$ with unbiased \hat{g} ,*

$$\mathbb{E}[(\tilde{g} - g)^2] = \eta^2 \text{Var}(\hat{g}) + (1 - \eta)^2 g^2.$$

If the cell size is n and $\text{Var}(\hat{g}) \leq \sigma^2/n$,

$$\mathbb{E}[(\tilde{g} - g)^2] \leq \eta^2 \frac{\sigma^2}{n} + (1 - \eta)^2 g^2.$$

Proof. Expanding,

$$(\tilde{g} - g)^2 = (\eta(\hat{g} - g) + (1 - \eta)(-g))^2 = \eta^2(\hat{g} - g)^2 + (1 - \eta)^2 g^2 - 2\eta(1 - \eta)g(\hat{g} - g).$$

Taking expectations and using $\mathbb{E}[\hat{g} - g] = 0$, the cross term vanishes, yielding the claim. Substitute the variance bound for the second inequality. \square

Sample size rule

Theorem A.22 (Sufficient condition for uniform accuracy). *If for all single levels and pairs*

$$n_{\min} \geq \frac{2B^2}{\epsilon_1^2} \log\left(\frac{2\sum_{j < k} L_j L_k + 2\sum_j L_j}{\delta}\right),$$

then with probability $1 - \delta$,

$$\sup_{\ell} |\hat{g}_j(\ell) - g_j(\ell)| \leq \epsilon_1 + \epsilon_0, \quad \sup_{\ell, m} |\hat{g}_{jk}(\ell, m) - g_{jk}(\ell, m)| \leq 3\epsilon_1 + \epsilon_0.$$

For weighted estimation, replace n_{\min} with $n_{\text{eff}, \min}$.

Proof. Combine Corollary A.14 for uniform cell bounds with Theorem A.18 to propagate to effects. For weighted estimation, Proposition A.16 implies replacement by n_{eff} . \square

A.3 Monte Carlo Approximation and Propagation Bounds

We present concentration guarantees for the Monte Carlo estimation of Shapley values, and show how this estimation error propagates to the two-factor effect table and the objective function via linear algebraic expansions. Notation follows §3 and §5.

Definition A.23 (Monte Carlo Shapley estimation). For evaluation point x and factor j , define a single marginal contribution as

$$\Delta_j(x; \pi) := v(\text{Pre}_\pi(j) \cup \{j\}) - v(\text{Pre}_\pi(j)), \quad v(T) := \mathbb{E}[f(x_T, X_{-T})],$$

where π is drawn uniformly at random from permutations. The Monte Carlo estimator with M samples is

$$\hat{\phi}_j^{\text{MC}}(x) = \frac{1}{M} \sum_{s=1}^M \Delta_j(x; \pi_s).$$

The same bounds apply if subset-based sampling is used, provided the Δ_j are i.i.d.

Single-coordinate bounds

Lemma A.24 (Boundedness of marginal contributions). *If predictions are bounded $|f| \leq B$, then for all x, j, π , $|\Delta_j(x; \pi)| \leq 2B$.*

Proof. By definition,

$$\Delta_j(x; \pi) = \mathbb{E}[f(x_{S \cup \{j\}}, X_{-(S \cup \{j\})})] - \mathbb{E}[f(x_S, X_{-S})], \quad S := \text{Pre}_\pi(j).$$

Each expectation lies in $[-B, B]$, so their difference is at most $2B$ in magnitude. \square

Theorem A.25 (Hoeffding bound). *For any x, j and $\delta \in (0, 1)$,*

$$|\hat{\phi}_j^{\text{MC}}(x) - \phi_j(x)| \leq 2B \sqrt{\frac{2 \log(2/\delta)}{M}} \quad \text{with prob. } \geq 1 - \delta.$$

Proof. The samples $\Delta_j(x; \pi_s)$ are i.i.d. and lie in $[-2B, 2B]$. Applying Hoeffding's inequality,

$$\Pr\left(|\hat{\phi}_j^{\text{MC}}(x) - \phi_j(x)| \geq t\right) \leq 2 \exp\left(-\frac{2Mt^2}{(4B)^2}\right).$$

Setting the right-hand side equal to δ and solving for t yields the result. \square

Corollary A.26 (Uniform bound over multiple coordinates). *For an evaluation set \mathcal{E} ,*

$$\max_{x \in \mathcal{E}} \max_{1 \leq j \leq d} |\hat{\phi}_j^{\text{MC}}(x) - \phi_j(x)| \leq 2B \sqrt{\frac{2 \log(2d|\mathcal{E}|/\delta)}{M}} \quad \text{with prob. } \geq 1 - \delta.$$

Proof. Apply Theorem A.25 to each (x, j) pair and use a union bound. \square

Linear propagation to effect tables

Definition A.27 (Linear model and design matrix). Under the independent product distribution assumption, $\phi_j(x) = g_j(x_j) + \frac{1}{2} \sum_{k \neq j} g_{jk}(x_j, x_k)$. On evaluation set \mathcal{E} , define the observation vector

$$\Phi := (\phi_j(x))_{x \in \mathcal{E}, 1 \leq j \leq d} \in \mathbb{R}^N, \quad N = d|\mathcal{E}|,$$

and the unknown parameter vector

$$\theta := (g_j(\ell))_{j, \ell} \oplus (g_{jk}(\ell, m))_{j < k, \ell, m} \in \mathbb{R}^p.$$

Then the system is linear: $\Phi = A\theta$. Each row of A encodes the contribution of a single (x, j) , with entries of 1 for relevant main effects, 1/2 for interactions involving j , and zeros otherwise. Centering constraints are imposed separately.

Proposition A.28 (Least-squares recovery and stability). *Suppose $\sigma_{\min}(A) > 0$. For Monte Carlo estimates $\hat{\Phi}$, the least-squares solution*

$$\hat{\theta} := \arg \min_{\theta} \|A\theta - \hat{\Phi}\|_2^2$$

satisfies

$$\|\hat{\theta} - \theta\|_2 \leq \frac{1}{\sigma_{\min}(A)} \|\hat{\Phi} - \Phi\|_2,$$

and thus $\|\hat{\theta} - \theta\|_{\infty} \leq \|\hat{\theta} - \theta\|_2$.

Proof. From the normal equations,

$$\hat{\theta} - \theta = (A^{\top}A)^{-1}A^{\top}(\hat{\Phi} - \Phi).$$

The operator norm is bounded as $\|(A^{\top}A)^{-1}A^{\top}\|_2 = 1/\sigma_{\min}(A)$. The ℓ_{∞} bound follows since $\|\cdot\|_{\infty} \leq \|\cdot\|_2$. \square

Theorem A.29 (Uniform error in effect tables). *Under Corollary A.26,*

$$\|\hat{\Phi} - \Phi\|_2 \leq \sqrt{N} 2B \sqrt{\frac{2 \log(2N/\delta)}{M}} \quad \text{with prob. } \geq 1 - \delta.$$

Hence, letting $C_A := \sigma_{\min}(A)^{-1}$,

$$\begin{aligned} \max_{j, \ell} |\hat{g}_j(\ell) - g_j(\ell)| &\leq C_A 2B \sqrt{\frac{2N \log(2N/\delta)}{M}}, \\ \max_{j < k, \ell, m} |\hat{g}_{jk}(\ell, m) - g_{jk}(\ell, m)| &\leq C_A 2B \sqrt{\frac{2N \log(2N/\delta)}{M}}. \end{aligned}$$

Proof. If every component error is at most t , then the ℓ_2 error is bounded by $\sqrt{N}t$. Applying Corollary A.26 with $N = d|\mathcal{E}|$ gives the bound on $\|\hat{\Phi} - \Phi\|_2$. Proposition A.28 then transfers this to parameter components. \square

Propagation to the approximation and objective

Theorem A.30 (Deviation of approximation and objective). *If the risk penalty and cost terms do not depend on Monte Carlo estimation, then*

$$\sup_{x \in \Omega} |\hat{J}(x) - J(x)| \leq \sum_j \max_{\ell} |\hat{g}_j(\ell) - g_j(\ell)| + \sum_{j < k} \max_{\ell, m} |\hat{g}_{jk}(\ell, m) - g_{jk}(\ell, m)|.$$

Consequently, with $C := C_A 2B \sqrt{2N \log(2N/\delta)}$,

$$\sup_{x \in \Omega} |\hat{J}(x) - J(x)| \leq C M^{-1/2} \quad \text{with prob. } \geq 1 - \delta.$$

Proof. From the definition $\tilde{f} = \mu + \sum_j g_j(x_j) + \sum_{j < k} g_{jk}(x_j, x_k)$, the triangle inequality yields the bound on $|\hat{f}(x) - \tilde{f}(x)|$. Substituting into $J = \tilde{f} - \text{risk} - \text{cost}$ and applying Theorem A.29 completes the proof. \square

Lemma A.31 (Guarantee of near-optimality). *If $\sup_{x \in \Omega} |\hat{J}(x) - J(x)| \leq \varepsilon$, then*

$$J(\hat{x}^*) \geq J(x^*) - 2\varepsilon, \quad \hat{x}^* \in \arg \max_x \hat{J}(x), \quad x^* \in \arg \max_x J(x).$$

Proof. We have $J(\hat{x}^*) \geq \hat{J}(\hat{x}^*) - \varepsilon \geq \hat{J}(x^*) - \varepsilon \geq J(x^*) - 2\varepsilon$. The first and third inequalities follow from the uniform deviation assumption, and the middle inequality from optimality of \hat{x}^* . \square

Remark on subset sampling If marginal contributions are constructed from uniformly drawn subsets rather than permutations, the samples remain bounded and i.i.d., so Theorem A.25 and Corollary A.26 continue to hold. The only difference lies in the construction of the design matrix A . Ensuring $\sigma_{\min}(A) > 0$ requires selecting evaluation points and subset designs rich enough to excite all effect terms.

A.4 Coordinate Ascent and Optimality Guarantees

This section develops the properties of coordinate-based optimizers, including monotonicity, finite termination, 1-swap optimality, and global optimality under diagonal dominance. The combination space is a finite set $\Omega \subseteq \prod_{j=1}^d \mathcal{L}_j$ and the objective function is

$$J(x) = \tilde{f}(x) - \lambda_{\text{risk}} \mathcal{R}(x) - \lambda_{\text{cost}} C(x).$$

For notational simplicity, define the local objective when changing coordinate j as

$$F_j(\ell | x) := \tilde{g}_j(\ell) + \sum_{k \neq j} \tilde{g}_{jk}(\ell, x_k) - \lambda_{\text{risk}} \sum_{k \neq j} r_{jk}(\ell, x_k) - \lambda_{\text{cost}} \Delta C_j(\ell | x),$$

where $\Delta C_j(\ell | x) = C(x_{-j}, \ell) - C(x)$. A coordinate update step is then

$$x_j^+ \in \arg \max_{\ell \in \mathcal{L}_j, (x_{-j}, \ell) \in \Omega} F_j(\ell | x), \quad x^+ = (x_{-j}, x_j^+).$$

Lemma A.32 (Monotonicity). *For any $x \in \Omega$ and coordinate j ,*

$$J(x^+) - J(x) = F_j(x_j^+ | x) - F_j(x_j | x) \geq 0.$$

Equality holds only when x_j is already locally optimal.

Proof. Comparing only the terms of J that involve coordinate j ,

$$\begin{aligned} J(x^+) - J(x) &= \left\{ \tilde{g}_j(x_j^+) - \tilde{g}_j(x_j) \right\} + \sum_{k \neq j} \left\{ \tilde{g}_{jk}(x_j^+, x_k) - \tilde{g}_{jk}(x_j, x_k) \right\} \\ &\quad - \lambda_{\text{risk}} \sum_{k \neq j} \left\{ r_{jk}(x_j^+, x_k) - r_{jk}(x_j, x_k) \right\} - \lambda_{\text{cost}} \left\{ C(x_{-j}, x_j^+) - C(x) \right\}. \end{aligned}$$

The right-hand side is exactly $F_j(x_j^+ | x) - F_j(x_j | x)$, which is nonnegative by definition of x_j^+ . \square

Proposition A.33 (Finite termination). *Starting from any $x^{(0)} \in \Omega$, repeated coordinate sweeps terminate in finitely many steps.*

Proof. Since Ω is finite, Lemma A.32 implies that J strictly increases whenever an update occurs. To avoid cycles of equal value, fix a deterministic lexicographic tie-breaking rule. Then iterations continue only if J increases, and thus termination occurs in finitely many steps. \square

Definition A.34 (1-swap optimality). $\hat{x} \in \Omega$ is 1-swap optimal if for all j and all $\ell \in \mathcal{L}_j$ with $(\hat{x}_{-j}, \ell) \in \Omega$, we have $J(\hat{x}) \geq J(\hat{x}_{-j}, \ell)$.

Proposition A.35 (1-swap optimality of fixed points). *When the procedure of Proposition A.33 terminates, the resulting \hat{x} is 1-swap optimal.*

Proof. At termination, for each j , changing x_j cannot increase J . By Lemma A.32, all possible updates yield nonpositive improvements, which is exactly the definition of 1-swap optimality. \square

Diagonal dominance and global optimality Define the minimal margin of improvement for coordinate j as

$$m_j := \min_{\substack{\ell \neq \ell' \\ (x_{-j}, \ell), (x_{-j}, \ell') \in \Omega}} \left\{ F_j(\ell | x) - F_j(\ell' | x) \right\}_+.$$

Define the maximum influence of coordinate k on the local objective of coordinate j as

$$L_{jk} := \sup_{\substack{\ell \in \mathcal{L}_j \\ x_{-j}, y_{-j}: x_{-j} \equiv y_{-j} \text{ except on } k}} \left| F_j(\ell | x) - F_j(\ell | y) \right|.$$

Diagonal dominance holds if $\sum_{k \neq j} L_{jk} < m_j$ for all j .

Lemma A.36 (Contraction of best responses). *Under diagonal dominance, for any contexts $x, y \in \Omega$ and any j ,*

$$F_j(B_j(y) | y) - F_j(B_j(x) | y) \leq \sum_{k \neq j} L_{jk} \mathbf{1}\{x_k \neq y_k\},$$

where $B_j(\cdot)$ denotes the best-response operator for coordinate j . In particular,

$$F_j(B_j(x) | x) - F_j(B_j(y) | x) \geq m_j - \sum_{k \neq j} L_{jk} \mathbf{1}\{x_k \neq y_k\}.$$

Proof. The first inequality follows from the Lipschitz-type condition on $F_j(\ell | \cdot)$. The second inequality uses that $B_j(x)$ is optimal in context x , combined with the first inequality for $\ell = B_j(x)$. \square

Theorem A.37 (Global optimality and uniqueness). *If diagonal dominance holds, the coordinate ascent procedure converges to a unique fixed point x^* independent of initialization, and $x^* \in \arg \max_{x \in \Omega} J(x)$.*

Proof. Let the Hamming distance be $d_H(x, y) = \sum_j \mathbf{1}\{x_j \neq y_j\}$. Denote one full sweep of updates by T . By Lemma A.36, each coordinate update reduces contextual differences by a factor of at most $\sum_{k \neq j} L_{jk} / m_j$. Under diagonal dominance this factor is strictly less than 1, so T is a contraction mapping with a unique fixed point. Iterative updates converge to this fixed point x^* . Since x^* is 1-swap optimal and under diagonal dominance all local maxima are global maxima, it follows that x^* is the unique global maximizer. \square

Corollary A.38 (Order-invariant convergence). *If diagonal dominance holds, convergence is independent of the order of coordinate updates.*

Proof. Theorem A.37 already establishes uniqueness of the fixed point, which implies order-invariance. \square

Role of constraints The above conditions apply whenever Ω is a finite feasible set with candidate levels for each coordinate. If constraints make some levels infeasible for certain contexts x_{-j} , then m_j and L_{jk} are defined with feasibility restrictions. Diagonal dominance is thus interpreted relative to feasible contexts.

Guarantees under approximate objectives

Lemma A.39 (Uniform deviation and optimality gap). *If $\sup_{x \in \Omega} |\hat{J}(x) - J(x)| \leq \varepsilon$, then*

$$J(\hat{x}^*) \geq J(x^*) - 2\varepsilon, \quad \hat{x}^* \in \arg \max_x \hat{J}(x), \quad x^* \in \arg \max_x J(x).$$

Proof.

$$J(\hat{x}^*) \geq \hat{J}(\hat{x}^*) - \varepsilon \geq \hat{J}(x^*) - \varepsilon \geq J(x^*) - 2\varepsilon.$$

The first and third inequalities follow from the uniform deviation assumption, while the middle inequality follows from optimality of \hat{x}^* . \square

Strengthening with two-coordinate moves In practice, a 1-swap optimal point need not be globally optimal. Allowing two-coordinate moves yields the following bound.

Proposition A.40 (Improvement bound from two-coordinate moves). *For any 1-swap optimal \hat{x} and any $y \in \Omega$,*

$$\begin{aligned} J(y) - J(\hat{x}) &\leq \sum_{j < k} \left\{ \max_{\ell, m} [\tilde{g}_{jk}(\ell, m) - \tilde{g}_{jk}(\hat{x}_j, \hat{x}_k)]_+ \right\} + \sum_j \max_{\ell} [\tilde{g}_j(\ell) - \tilde{g}_j(\hat{x}_j)]_+ \\ &\quad + \lambda_{\text{risk}} \sum_{j < k} [r_{jk}(\hat{x}_j, \hat{x}_k) - \min_{\ell, m} r_{jk}(\ell, m)]_+ + \lambda_{\text{cost}} \sum_j [\Delta C_j(\hat{x}_j | \hat{x})]_+. \end{aligned}$$

In particular, under strong diagonal dominance the right-hand side is small, implying that the gap between a 1-swap optimum and the global optimum is limited.

Proof. Expand $J(y) - J(\hat{x})$ into differences of main effects, interactions, risk, and cost. Each difference is bounded by its maximum possible increase. The notation $[a]_+ = \max(a, 0)$ collects these increases into the stated bound. \square

Summary Coordinate ascent always increases J monotonically and terminates in finite steps. The resulting point is 1-swap optimal, and under diagonal dominance it is the unique global optimum. Even with approximate objectives, a uniform deviation of ε guarantees the solution's value is within 2ε of the global optimum. Allowing two-coordinate moves further narrows the possible gap between local and global optima.

A.5 Properties and Auxiliary Results of PCI

The PCI standardizes interaction matrices into dimensionless form, enabling comparisons both within and across factor pairs. Here we summarize properties including centering, symmetry, scale invariance, energy normalization, range of maxima, effects under shrinkage, and interpretation in separable structures. Notation follows §3 and §5.

Definition A.41 (PCI and normalization constant). For a factor pair (j, k) and level pair (ℓ, m) ,

$$\text{PCI}_{jk}(\ell, m) := \frac{g_{jk}(\ell, m)}{s_{jk}}, \quad s_{jk} := \left(\frac{1}{L_j L_k} \sum_{\ell', m'} g_{jk}(\ell', m')^2 \right)^{1/2}.$$

If $s_{jk} = 0$, then $g_{jk} \equiv 0$ and we set $\text{PCI}_{jk} \equiv 0$.

Lemma A.42 (Properties of the normalization constant). *We have $s_{jk} \geq 0$, and $s_{jk} = 0$ if and only if $g_{jk}(\ell, m) = 0$ for all (ℓ, m) .*

Proof. By definition the denominator is the square root of an average of squares, which is nonnegative and equals zero only when all terms vanish. \square

Proposition A.43 (Symmetry and centering). *For all (j, k, ℓ, m) ,*

$$\text{PCI}_{jk}(\ell, m) = \text{PCI}_{kj}(m, \ell).$$

Moreover, double centering is preserved: $\sum_m \pi_{k|j}(m | \ell) \text{PCI}_{jk}(\ell, m) = 0$ for all ℓ , and $\sum_{\ell} \pi_{j|k}(\ell | m) \text{PCI}_{jk}(\ell, m) = 0$ for all m .

Proof. Symmetry follows from $g_{jk}(\ell, m) = g_{kj}(m, \ell)$ and $s_{jk} = s_{kj}$. Centering holds because the positive constant s_{jk} cancels, leaving the centering condition of g_{jk} . \square

Proposition A.44 (Invariance under scaling and translation). *For constants a, b , let $f^* = af + b$. Then*

$$g_{jk}^* = a g_{jk}, \quad s_{jk}^* = |a| s_{jk}.$$

Hence if $a > 0$, $\text{PCI}_{jk}^ = \text{PCI}_{jk}$. If $a < 0$, the sign flips. The constant shift b has no effect on g_{jk} .*

Proof. By linearity, interactions scale by a . The normalization constant scales by $|a|$. Thus the ratio is preserved up to sign. \square

Proposition A.45 (Energy normalization and range of maxima). *For any (j, k) ,*

$$\sum_{\ell, m} \text{PCI}_{jk}(\ell, m)^2 = L_j L_k.$$

Furthermore,

$$1 \leq \max_{\ell, m} |\text{PCI}_{jk}(\ell, m)| \leq \sqrt{L_j L_k}.$$

Proof. Vectorizing $u \in \mathbb{R}^{L_j L_k}$ as $u_{\ell m} = g_{jk}(\ell, m)$, we have $s_{jk} = \|u\|_2 / \sqrt{L_j L_k}$. Then $p_{\ell m} = u_{\ell m} / s_{jk}$ satisfies

$$\sum_{\ell, m} p_{\ell m}^2 = \frac{\|u\|_2^2}{s_{jk}^2} = L_j L_k.$$

The lower bound follows since the mean square equals 1, hence the maximum absolute value cannot be less than 1. The upper bound follows from $\|p\|_\infty \leq \|p\|_2 = \sqrt{L_j L_k}$. \square

Proposition A.46 (Effect of uniform shrinkage). *If $\tilde{g}_{jk} = \eta g_{jk}$ with constant $\eta \in (0, 1]$, then $\tilde{s}_{jk} = \eta s_{jk}$ and PCI remains unchanged.*

Proof. Multiplying numerator and denominator by the same factor leaves the ratio invariant. \square

Proposition A.47 (Effect of cellwise shrinkage). *Let $\tilde{g}_{jk}(\ell, m) = \eta_{\ell m} g_{jk}(\ell, m)$ with coefficients $\eta_{\ell m} \in (0, 1]$. Define the weighted average $\tilde{\eta}_u^2 = \frac{\sum_{\ell, m} \eta_{\ell m}^2 g_{jk}(\ell, m)^2}{\sum_{\ell, m} g_{jk}(\ell, m)^2}$. Then*

$$\tilde{s}_{jk} = \sqrt{\tilde{\eta}_u^2} s_{jk}, \quad \text{PCI}_{jk}^{\sim}(\ell, m) = \frac{\eta_{\ell m}}{\sqrt{\tilde{\eta}_u^2}} \text{PCI}_{jk}(\ell, m).$$

If $\eta_{\min} \leq \eta_{\ell m} \leq \eta_{\max}$, then

$$\left| \text{PCI}_{jk}^{\sim}(\ell, m) - \text{PCI}_{jk}(\ell, m) \right| \leq \left(\max \left\{ \frac{\eta_{\max}}{\eta_{\min}} - 1, 1 - \frac{\eta_{\min}}{\eta_{\max}} \right\} \right) |\text{PCI}_{jk}(\ell, m)|.$$

Proof. The first identity follows from the definition of the normalization constant with $\eta_{\ell m}^2$. The second identity results from division. Since $\tilde{\eta}_u \in [\eta_{\min}, \eta_{\max}]$, the ratio $\eta_{\ell m} / \tilde{\eta}_u$ lies in $[\eta_{\min} / \eta_{\max}, \eta_{\max} / \eta_{\min}]$. Taking the maximal absolute deviation yields the inequality. \square

Proposition A.48 (PCI under separable interactions). *Suppose $g_{jk}(\ell, m) = a_j(\ell) b_k(m)$ with $\sum_{\ell} \pi_j(\ell) a_j(\ell) = 0$ and $\sum_m \pi_k(m) b_k(m) = 0$. Then*

$$s_{jk} = \left(\mathbb{E}[a_j(X_j)^2] \mathbb{E}[b_k(X_k)^2] \right)^{1/2}, \quad \text{PCI}_{jk}(\ell, m) = \frac{a_j(\ell)}{\sqrt{\mathbb{E}[a_j(X_j)^2]}} \cdot \frac{b_k(m)}{\sqrt{\mathbb{E}[b_k(X_k)^2]}}.$$

Thus the PCI matrix has the structure of an outer product between a row vector and a column vector.

Proof. Expanding the sum of squares gives $\sum_{\ell, m} g_{jk}(\ell, m)^2 = (\sum_{\ell} a_j(\ell)^2) (\sum_m b_k(m)^2)$. Computing the normalization constant and the ratio yields the stated form. \square

Remark A.49 (Weighted normalization variant). *If a weighted average is used instead of a uniform average,*

$$s_{jk, w} = \left(\sum_{\ell, m} \pi_{jk}(\ell, m) g_{jk}(\ell, m)^2 \right)^{1/2},$$

then centering and scale invariance still hold, and energy normalization becomes $\sum \pi_{jk} \text{PCI}_{jk, w}^2 = 1$.

Remark A.50 (Summary of interpretation). *PCI preserves symmetry and centering, remains stable under positive scaling and translation, and its normalization fixes the total sum of squares to the number of cells, allowing relative strength comparisons across factor pairs. Uniform shrinkage leaves PCI unchanged, while cellwise shrinkage rescales contributions level by level. Under separable structures, PCI matrices reveal standardized row and column signals in outer product form.*

B Visualization of Main Effects and Interactions

This section collects the main-effect and interaction plots in one place. All metrics are aligned so that higher values indicate better performance, and effect sizes are standardized within each dataset for comparability. Panels are organized in the order: UCI Concrete (Figures 3, 6), UCI Car Evaluation (Figures 4, 7), and Fashion MNIST (Figures 5, 8).

Consistent directional patterns emerge across datasets. The Adam optimizer dominates in all cases. Higher learning-rate levels repeatedly show monotone improvements. Smaller batch sizes strongly correlate with higher performance. Weight decay (L_2) exerts weak or nearly flat effects, while increasing the number of epochs produces gradual gains. Confidence intervals are well separated in Concrete and Car, but differences narrow in FMNIST, where effect magnitudes are smaller overall.

For UCI Concrete, main effects are pronounced. Performance is highest when Adam, high learning rate, and small batch size are combined, while L_2 remains almost flat (Figure 3). Among interactions, learning rate–batch size is strongest, followed by optimizer–learning rate. In both pairs, slope and spacing change together, breaking parallelism (Figure 6).

In UCI Car Evaluation, the same pattern holds. Monotone gains from learning rate are even clearer, and batch effects are distinct (Figure 4). The interaction ranking is again led by learning rate–batch size, followed by optimizer–learning rate, while L_2 -related combinations remain weak (Figure 7).

For Fashion MNIST, overall effect sizes are smaller. Adam’s advantage and the benefit of small batch size remain but with narrower gaps, and the learning-rate effect is milder (Figure 5). Interactions are generally weak, with L_2 -related curves nearly overlapping (Figure 8).

In summary, learning rate and batch size are the primary factors, optimizer is secondary, epochs play a supporting role, and L_2 ranks lowest. The recommended baseline is Adam, high learning rate, small batch size, weak L_2 , and a moderate number of epochs. Exploration should sweep learning rate and batch size over a broad grid first, then refine locally near the optimum. Optimizer changes should be tested only when gaps are small, L_2 should be tuned narrowly, and epochs increased gradually until plateau, with early stopping enabled.

Caveats are also noted. Small batch size is not universally optimal: in memory-constrained or preprocessing-bottlenecked environments, intermediate batch sizes may be more stable. When improvements occur only at high learning rates, combined effects with schedulers should be checked. Although L_2 appears flat, extreme values may trigger numerical instability, so safe ranges must be specified. All conclusions are supported by multi-seed averages with confidence intervals.

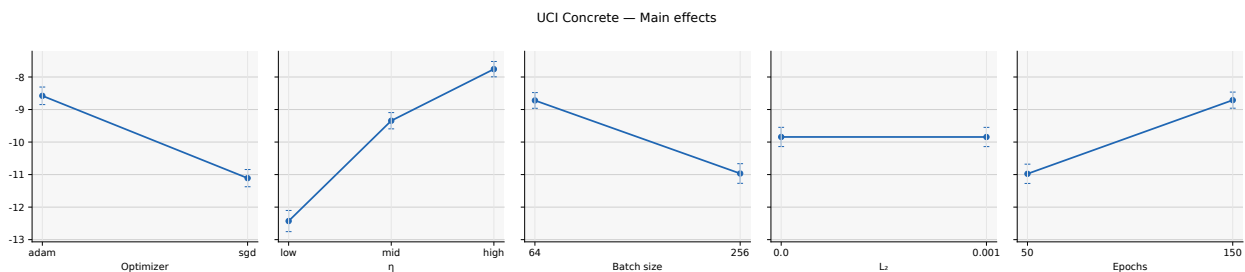


Figure 3: UCI Concrete — Main effects.

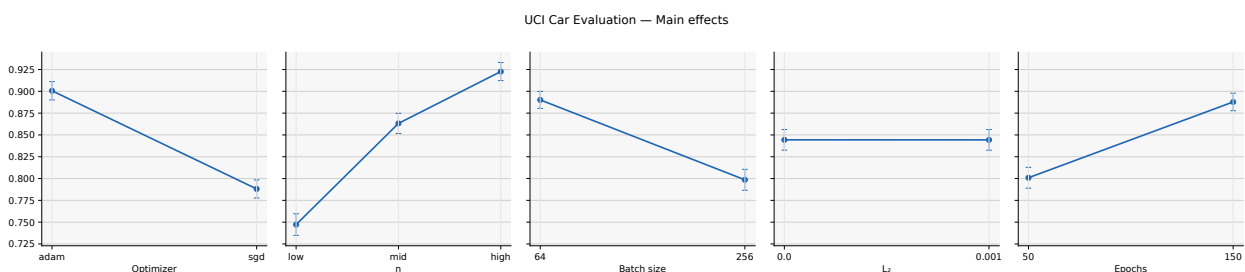


Figure 4: UCI Car Evaluation — Main effects.

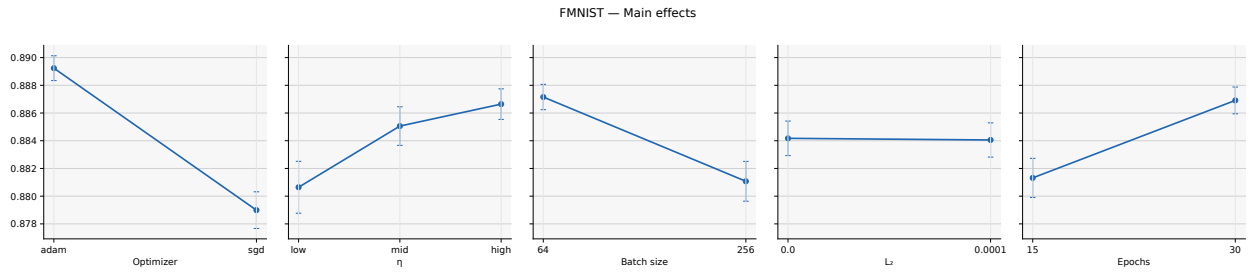


Figure 5: Fashion MNIST — Main effects.

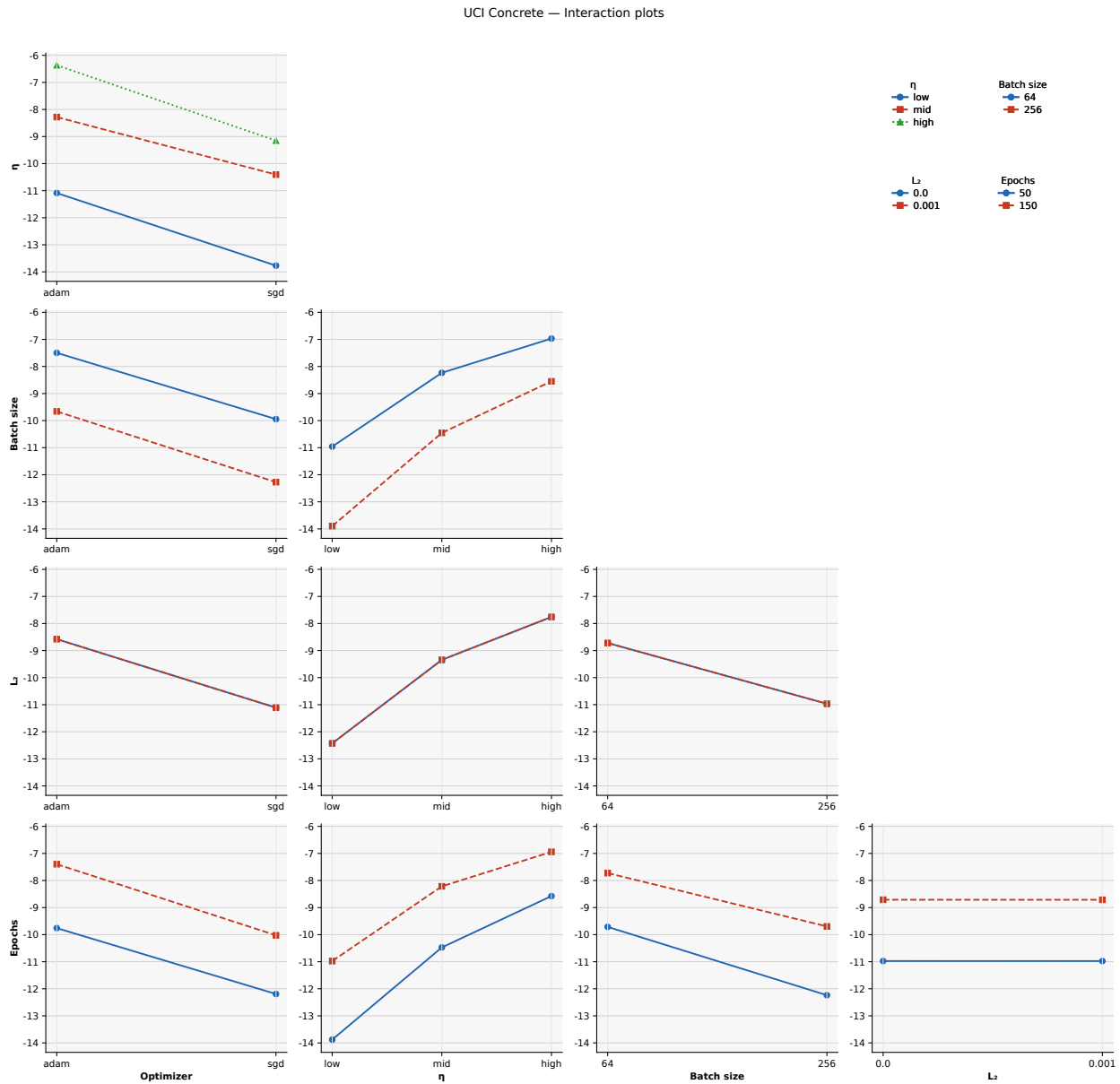


Figure 6: UCI Concrete — Interactions.

UCI Car Evaluation — Interaction plots

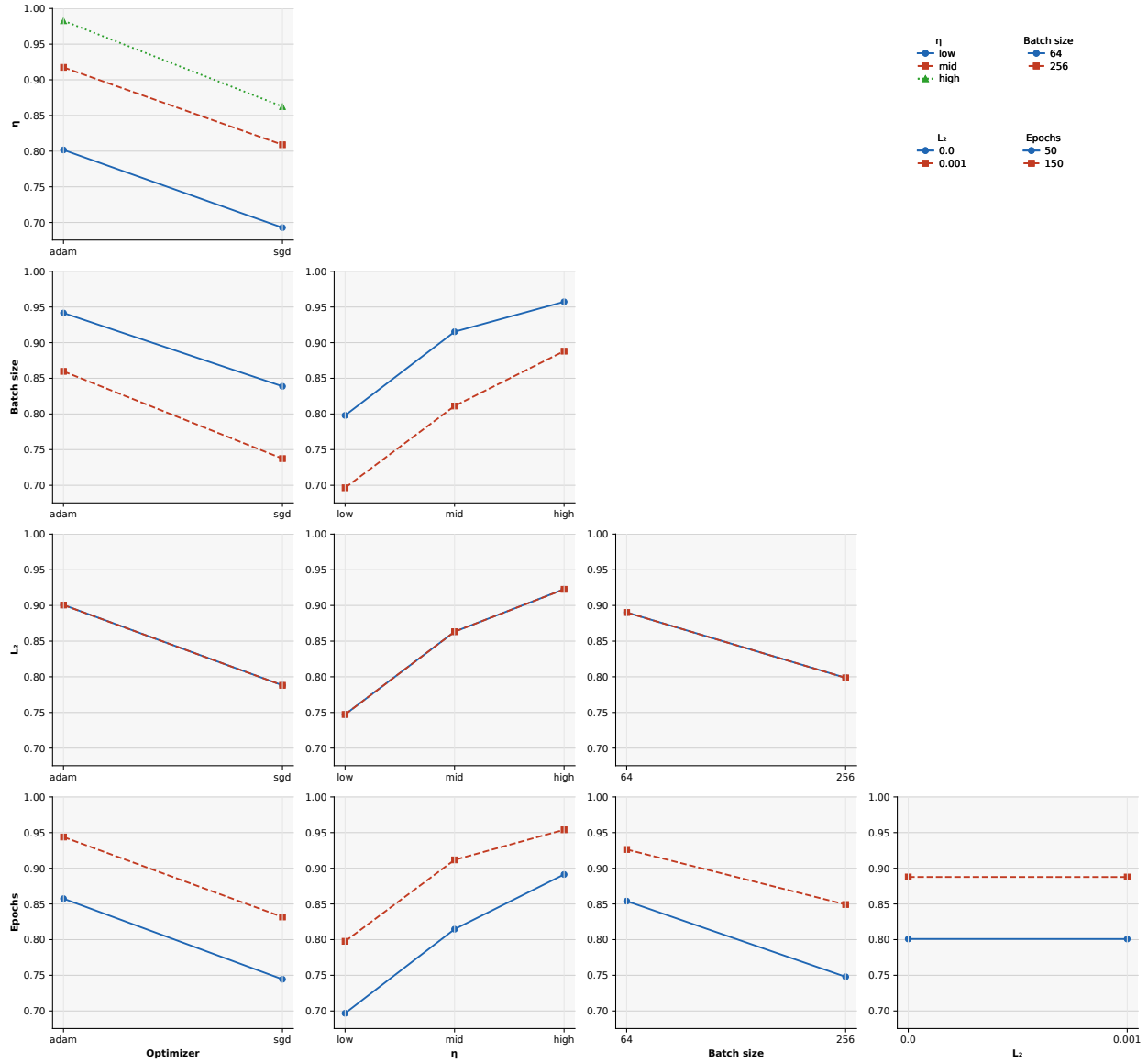


Figure 7: UCI Car Evaluation — Interactions.

FMNIST — Interaction plots

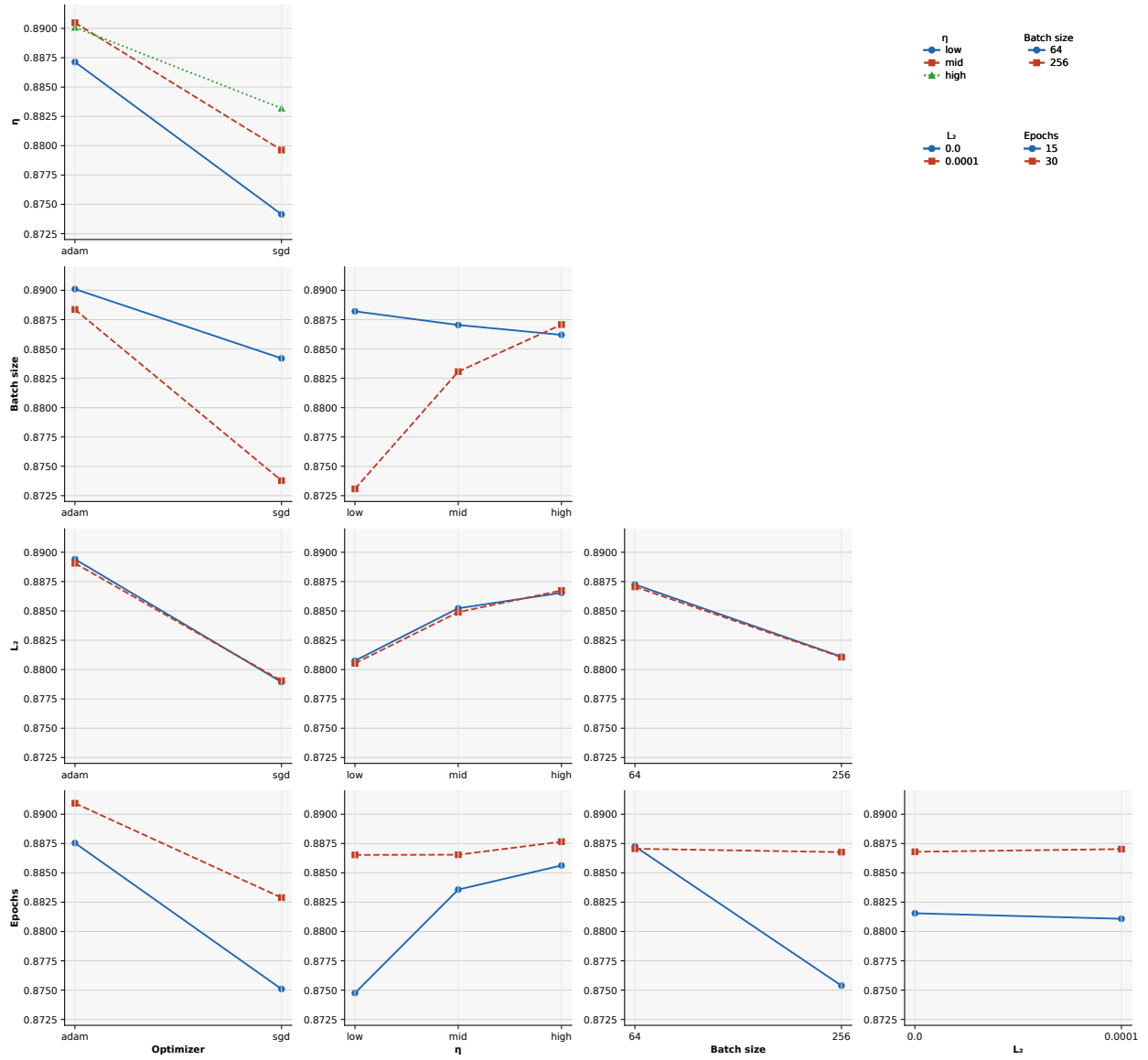


Figure 8: Fashion MNIST — Interactions.

C Ethics and Policy

This section outlines the ethical principles and operational guidelines for deploying FACTORS in practice. The goal is to achieve both performance improvements and trust. Adjustment procedures based on main and interaction effects are standardized, and the risk-adjusted score and budget rules are linked to transparent decision processes to ensure reproducibility, proportionality, and safeguards against misuse.

Purpose and scope FACTORS evaluates combinations of training factors such as learning rate, batch size, regularization strength, and schedule, without altering the underlying data. As such, the focus lies on operational choices and risk management rather than on privacy concerns. The principles below establish minimum standards to align operational decisions with institutional requirements.

Risk management and proportionality The risk-adjusted score is defined as expected performance minus penalties for uncertainty and cost. In early deployment, risk aversion should be set conservatively and then gradually relaxed as validation data and service risk profiles are monitored. High-impact changes must be rolled out in stages with monitoring, predefined rollback rules, and proportional interventions relative to expected risks and potential benefits.

Transparency, documentation, and auditability All experiments and pre-/post-deployment decisions must record: (i) design summary with seeds and sample sizes; (ii) main and interaction effect estimates with standard errors; (iii) cost and budget usage; and (iv) timestamps and responsible personnel for approvals and deployments. These records should be directly usable for internal reviews and external audits.

Reproducibility and technical debt minimization Code, configurations, seeds, and data paths must be fixed to ensure that results are exactly reproducible. Unit tests and continuous integration should monitor regressions, and the structure of experiment outputs and logs must remain consistent to avoid technical debt accumulation.

Fairness and non-discrimination Relative comparisons across factor combinations must not obscure subgroup disparities. Key subgroup metrics must be reported alongside overall results. Combinations that worsen performance for specific groups should be excluded or assigned higher risk aversion. If subgroup gaps exceed organizational thresholds, deployment must be suspended pending alternatives.

Data protection and log minimization Reproducibility experiments should use public or de-identified data where possible. Operational logs must not contain information that can identify individuals, customers, or organizations. Access must follow the principle of least privilege, retention periods must be strictly limited to operational necessity, and external artifacts should include only metadata required for reproduction.

Stability safeguards When residuals or higher-order interactions not explained by the two-factor approximation are observed, additional diagnostics must be performed. Model complexity should be expanded only step by step, with effect estimates, projection residuals, distribution choices, and budget usage reported together to control overfitting and bias.

Operational thresholds and rollback If optimality gaps, rank preservation metrics, or uncertainty bounds exceed thresholds, deployment must be halted. After deployment, performance, stability, and fairness indicators should be continuously monitored over predefined windows. Exceeding thresholds should trigger automatic rollback and re-adjustment.

Misuse prevention and usage boundaries FACTORS results must not be used as grounds for inappropriate evaluation or sanctions against individuals or groups. The tool is designed solely to support technical choices in model operations. Organizational-level rewards or sanctions must undergo independent ethical and legal review.

Stakeholder communication Shared summary reports for model owners, operators, validators, and reviewers should include selected configurations and alternatives, risks and costs, budget usage, fairness and stability diagnostics, and operational thresholds and rollback rules. When results are externally disclosed, reports must also specify methods, data, constraints, limitations, and reproduction procedures.

Checklist summary Apply standardized design and logging practices. Start with conservative risk and cost weights. Report subgroup performance and uncertainty jointly. Increase model complexity only where residuals indicate necessity. Do not deploy if threshold checks fail. After deployment, automate monitoring and rollback. Use testing and continuous

integration to preserve reproducibility and quality. Adhere consistently to principles of accountability, transparency, and documentation.

Limitations and disclaimer FACTORS relies on two-factor approximation and local stationarity assumptions. In environments with abrupt distribution shifts or dominant higher-order interactions, results must be interpreted conservatively. Adequate local validation is required before deployment, and extensions should be introduced only gradually as needed.